Partitioning of Indium Between Pyrrhotite and Silicate Melt

Sean Kayser GEOL 394 Nov 27th, 2013

Advisors:

Dr. Philip Candela Dr. Philip Piccoli

Abstract

The proportion of ore metals sequestered in crystallizing magmatic phases can be lost from a potentially ore-forming, magmatic-hydrothermal system. In order to shed light on this problem in the case of indium the partitioning of In between pyrrhotite and silicate melt has been determined in experiments at 800 °C, 100 MPa, and $fO_2 \approx NNO$ in a pyrrhotite-saturated, vapor-brine-silicate melt system. Three separate series of experiments were conducted in which each series differed by the aqueous solution added. The first series of experiments were prepared with pure water, the second series of experiments with a 1.01 M chloride solution and the third series with a 0.35 M CuCl₂-bearing aqueous solution. These changes in starting material produced changes in the composition of the run product pyrrhotite and glass. Crystals of pyrrhotite, along with quenched glasses, were

bearing aqueous solution. These changes in starting material produced changes in the composition of the run product pyrrhotite and glass. Crystals of pyrrhotite, along with quenched glasses, were analyzed by EPMA after 5, 10 and 15 day experiments. The $\overline{D_{\text{In}}^{\frac{P_0}{\text{melt}}}}$ for the pure water series experiments is on the order of $\overline{D_{\text{In}}^{\frac{P_0}{\text{melt}}}} \approx 10$. The addition of chloride-bearing aqueous solution leads to a decrease in the $\overline{D_{\text{In}}^{\frac{P_0}{\text{melt}}}} \approx 1.5$. Copper (II) chloride-bearing series experiments yields a $\overline{D_{\text{In}}^{\frac{P_0}{\text{melt}}}} \approx 3$. Although the $\overline{D_{\text{In}}^{\frac{P_0}{\text{melt}}}}$ does vary depending upon the starting aqueous solution, the combination of these data sets indicates that the best estimate for the partition coefficient for individual between approximates that

Although the D_{ln}^{melt} does vary depending upon the starting aqueous solution, the combination of these data sets indicates that the best estimate for the partition coefficient for indium between pyrrhotite and silicate melt is on the order of 4. Using reasonable estimates of the mass fraction of pyrrhotite that crystallizes in crustal magmatic systems, I modeled the proportion of indium sequestered by pyrrhotite during fractional crystallization. Pyrrhotite sequesters less than 0.5% indium from a

crystallizing silicate melt because of the small magnitude of the $D_{\text{In}}^{\frac{Po}{\text{melt}}}$, and low modal abundances of pyrrhotite. Experimental and model results indicate that crystallization of pyrrhotite alone does not limit the capacity for a magmatic-hydrothermal system to yield an indium rich ore fluid.

In an effort to further explore the behavior of indium, I developed a model to examine the effects of the magmatic crystallization of rock-forming minerals on the partitioning of indium in a number of idealized magmas as well as estimate a probable upper limit for the concentration of indium in an evolving ore fluid. The rock types chosen to represent the idealized magmas included a hortonolite ferrogabbro from the Skaergaard intrusion, east Greenland which represents a melanocratic "granitic" rock, a magnetite-rich granodiorite, and ilmentite-rich granodiorite, the latter two modeled after granites from the Tokuwa batholith, Central Japan. Theoretical partition coefficients for indium between melt and crystalline phases as well as bulk partition coefficients for indium were calculated by using the modal abundance of minerals and measured concentrations of indium in certain minerals from the cited literature. A modified form of the Rayleigh fractionation equation was used to model the proportion of indium sequestered. To place an upper limit on the concentration of indium in an evolving ore fluid the proportion of indium not sequestered was partitioned into the water vapor phase, ignoring further crystallization. The parent melt in the model contains, initially, 1 wt% water and become vapor saturated at 6 wt% water. The model shows that for an evolving ore fluid the concentration of indium in the ore fluid will increase progressing from a ferromagnesian-rich basaltic system (0.56 ppm) to a magnetite-rich (2.2 ppm), and finally magnetiteabsent, ilmentite-bearing felsic system (4.2 ppm). The modeled indium concentrations for evolving ore fluid are in agreement with those observed in nature. Zhang et al., (2007) used LA-ICPMS to measure the concentration of indium in fluid inclusions (proposed as samples of indium ore fluid) present in quartz from varying indium-rich and-poor ore deposits in China and found the concentration of indium for a indium-rich ore deposit to be 1.9 to 4.1 ppm. This research suggests to explorationists that Zn ores associated with magnetite-poor intrusions may be prospective.

Table of Contents

List of Figures	i
List of Tables	ii
Introduction	
 Magmatic Hydrothermal Systems 	
 Indium Deposits 	
Partition Coefficients	5
 Objective 	
 Hypothesis	
Test of Hypothesis	7
Experimental Procedure	
Starting Materials	· 7
 Experimental Design 	8
 Experimental Controls	9
Demonstration of Equilibrium	10
 Analytical Techniques 	
Binocular Microscope	10
Electron Probe Microanalyzer	
Uncertainty of Analysis	11
Experimental Results	12
 Discussion 	
 Indium Sequestration by Pyrrhotite 	18
Other Hypotheses for Indium Sequestration in Magmas	19
Conclusion	23
References	24
 Appendices 	
 Appendix A: Detection limits for elements analyzed in glass and pyrrhotite 	27
Appendix B: Chemical composition of pyrrhotite starting material	
Appendix C: Composition of glass run products	
Appendix D:Composition of pyrrhotite run products	
Appendix E: University of Maryland Honor Pledge	
rr ·	

List of Figures

Figure 1	Temperature vs. wt% H2O phase assemblage diagram for synthetic granite composition	3
Figure 2	Plot of $\log fO_2$ (oxygen fugacity) versus $\log fS_2$ (sulfur fugacity) for the system Fe-O ₂ -S ₂ -SiO ₂	4
Figure 3	Calculated pyrrhotite/liquid partition coefficients for indium plotted against weight fraction of pyrrhotite that yields a bulk partition coefficient equal to one	6
Figure 4	Failed experimental gold capsule	8
Figure 5	Three separate plots of $D_{ln}^{\frac{Po}{melt}}$ vs. experimental duration for pure water, chloride-bearing, and copper-bearing experiments	17
Figure 6	The fraction of indium in felsic magma that is sequestered by pyrrhotite	18
Figure 7	The fraction of indium in magma that is sequestered by varying modal abundance of crystalline phases	21

List of Tables

Table 1	Composition of the glass used as starting material	10
Table 2	Summary of experimental conditions	13
Table 3	Analyses of major elements for glass run products	14
Table 4	Concentration of indium in run products (wt%) and calculated partition coefficient for indium between pyrrhotite and silicate melt	16
Table 5	The proportion of indium sequestered by pyrrhotite in felsic magma after 30% fractional crystallization	18
Table 6	Partition coefficient and concentration of indium in minerals comprising a hortonolite ferrogabbro of the Skaergaard intrusion, East Greenland	19
Table 7	Modal abundance of minerals comprising a magnetite-rich hornblende-biotite granodiorite	21
Table 8	Modal abundance of minerals comprising an ilmenite-rich hornblende-biotite granodiorite	22

Introduction

Human innovation has led to new uses for indium, including the development of liquid crystal displays (LCD's), architectural glass, and cathode-ray tubes. One of the main uses for indium is the production of indium tin oxide (ITO). ITO has two important properties; it is electrically conductive, and it is optically transparent. Touch screens and high-end LCD's are in high demand and their operation relies on these two properties. Given that, the demand for indium has increased three-fold from 1990 to 2005 (USGS). ITO constituted nearly two-thirds of total domestic indium use in 2002 and is the primary use that raises the demand for indium (Jorgenson, 2005).

Native indium is rarely found in nature. It is primarily produced from the fumes, dust, slags, and residues of zinc smelting (Schwarz-Schampera and Herzig, 2002). The primary ore deposits that source indium are massive sulfide deposits, granite-related vein deposits, and skarn deposits (Ishihara and Endo, 2007). The Kidd Creek deposit in Canada is an example of massive sulfide deposit with recoverable indium. The Kidd Creek deposit is estimated to contain 135Mt of ore at an average grade of 50 g/t indium (Schwarz-Schampera and Herzig, 2002). Granite related vein deposits are found in at Mount Pleasant, Canada and contain a total of 1.7 Mt indium grading 280g/t (Sinclair et al., 2006). Formation of these ore deposits is a consequence of the sum total of the magmatic, tectonic, chemical, and hydrologic processes operating in the Earth's crust (Englander, 2005).

The focus of this study is to understand the behavior of indium during magmatic-hydrothermal processes. In magmatic-hydrothermal systems fluids, generated during the crystallization of a magma, transport metals that are later deposited. Ore deposits formed by magmatic-hydrothermal processes have provided more than half the world's supply of copper and molybdenum (Hedenquist and Lowenstern, 1994). By studying indium in magmatic-hydrothermal systems, geologists may better understand the formation of indium-bearing ores and the distribution of indium throughout the crust and develop better models for the exploration of the deposits.

Magmatic-Hydrothermal Systems

The development of a magmatic-hydrothermal system begins with the shallow emplacement of an intermediate to felsic water-rich magma to shallow levels in the crust (Candela and Holland, 1986; Candela and Piccoli, 2005; Tattich, 2012). Basaltic magmas are initially generated by partial melting of the mantle at a mid-ocean ridge. Progressively, the basaltic melt crystallizes, is altered, and is eventually subducted below continental crust, inducing melting beneath the volcanic arc (Hedenquist and Lowenstern, 1994). The basaltic arc magma generated beneath the volcanic arc is buoyant and rises through the earth's mantle. Zones of weakness created by faulting are the primary paths the magma follows on its ascent through the crust. Assimilation processes that involve both old and juvenile crust have shown to be possibilities for magma evolution (Zellmer and Annen, 2008). As the magma passes upward through the crust, pieces of the country rock through which it passes may be broken off and assimilated by the magma. Over the course of the magma's evolution it becomes more felsic and may have been enriched in components such as oxidized sulfur, alkali metals, water, chlorine, and ore components (i.e. copper, tin, indium) (Hedenquist and Lowenstern, 1994). The oxidized

sulfur, chlorine and ore components are most likely from the original basalt. Alkali metals are acquired from the original basalt as well as melting of the lower crust.

However, to simply state that the basaltic magma evolved to felsic magma does not adequately explain the complex processes involved. The compositional diversity and evolution of magmas is generally attributable to crystal fractionation. As the melt temperature drops below the liquidus crystals begin to form in the system. If the crystals are removed from the magma, either physically or chemically, new melt compositions are generated from the primary magma. This process is known as crystal fractionation. Speer (1987) studied the evolution of aluminum, iron, and magnesium (AFM) assemblages in granitoid rocks of the Liberty Hill pluton. Speer found that the magma evolution started with clinopyroxene reacting with the melt to produce actinolite, then ferro-edenite. The amphibole ferro-edentite then reacted with the melt to produce biotite. Speer points out that the reaction [melt + hornblende = biotite] should be written as [melt 1 + hornblende = melt 2 + biotite] because the reaction would use the melt as both source and sink to complete the reaction therefore generating a melt with a different composition than before the reaction. Although it is common to observe the sequence [hornblende, biotite + hornblende, biotite] in differentiated granites it is not necessarily always the case. Equilibrium experiments performed by Naney (1983) show that the paragenetic crystallization sequence is strongly dependent on the water content of the system. Naney demonstrated that the crystallization sequences for a granite composition magma containing 0.5 wt% water and 5.0 wt% water at 200 MPa are: 0.5 wt% – orthopyroxene, plagioclase, alkali feldspar, clinopyroxene, quartz, biotite, clinopyroxene (resorbed), orthopyroxene (resorbed); and 5.0 wt% -orthopyroxene, biotite, clinopyroxene, orthopyroxene (resorbed), plagioclase, alkali feldspar, clinopyroxene (resorbed), and quartz.

As the magma evolves and rises through the earth's crust the earlier crystallizing phases can be removed from the magma, resulting in a more felsic magma. The crystallizing phases are physically removed from the magma via crystal settling/floating and inward crystallization. Crystal settling/floating is based on the idea that the crystals formed in the magma will have different densities than the magma. Crystals that have a higher density than the magma will sink and those with a lower density will float. Layers of crystals will accumulate either at the bottom or top of the magma layers. The crystals that are at the bottom layers of the higher density crystals are effectively removed from contact with the magma as well as the crystal layers that are atop of the lower density crystals. Inward crystallization occurs due to the country rock being much cooler than the magma. Since the country rock is cooler the outer portion of the magma will most likely crystallize from the outside inward. As crystals accumulate, layers will form and the earlier forming crystals will become removed from the magma.

Once the intermediate to felsic magma is emplaced, heat will be lost from the magma to the surrounding country rock and the magma will begin to crystallize dominantly anhydrous phases. Plagioclase, orthopyroxene, quartz, and alkali-feldspar are the main anhydrous phases to crystallize from a granodiorite or granite. As anhydrous minerals continue to crystallize the magma will become enriched in water, to the point where a discreet water-rich phase will form. The water present can exist as a vapor phase. When the vapor pressure equals the load pressure on the system, water bubbles will begin to form in the magma (Tattich 2012). The bubbles produced will be buoyant, and will tend to rise and concentrate in the carapace of the magma chamber (Candela, 1991). This exsolved vapor phase is commonly referred to as a Magmatic Volatile Phase (MVP). Based on experimentally determined values by Burnham (1979) the

solubility of water in a silicate melt at 100 MPa is~4 wt% water. A granitic magma with 4 wt % water, at 200 MPa, will crystallize one-third before it becomes vapor saturated at approximately 6 wt% water. The magma begins to crystallize at 1000° C and becomes vapor saturated at 700° C. This leaves two-thirds of the magma to crystallize between 700° C and the solidus (675° C) (figure 1). A granitic magma with 1 wt % water will crystallize over 80% before it becomes

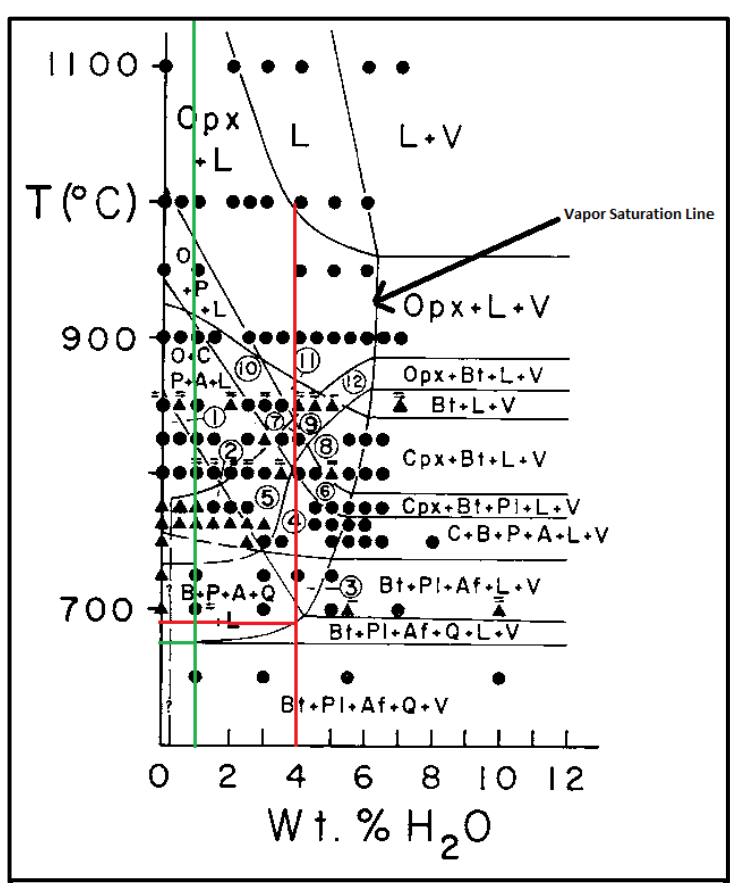


Figure 1. Temperature versus wt % H₂O phase assemblage diagram for synthetic granite compostion (R1 + 10Mi; 200 MPa) (Naney, 1983). The red line shows the path a magma with an intial four wt% H₂O will follow during crystallization. Two thirds of the melt will crystalize between 700° C and 675° C. The green line shows the path a magma with a intial one wt% water will follow during crystallization.

vapor saturated. The MVP that is exsolved from the magma can be a very efficient scavenger of metals. Holland (1972) showed that the partitioning of some metals (e.g. Cu, Zn) in water a magmatic temperature and pressure is dependent upon the concentration of chloride present in the MVP. Not all metals are capable of forming chloride complexes; therefore some metals will partition more readily than others. The complexing of indium with chloride at magmatic conditions has not been widely studied. Seward et al. (2000) studied indium chloride complexing between 25° C and 350° C and found that tetrachloroindium (InCl₄) is a significant transporter of indium in hydrothermal solutions and oreforming processes. Between 330° C and 350° C the InCl₄ complex contained greater than 95% of the total

The most common sulfide phase crystallizing from crustal magmas is pyrrhotite. Pyrrhotite constitutes a very small proportion of the total crystallizing assemblage. Candela (1986) and Whitney and Stormer, (1983), indicate that pyrrhotite is a common inclusion within phenocrystic phases in volcanic

indium in solution.

rocks. The evidence suggests that pyrrhotite is present as a supersolidus phase at the time of magma generation. Experiments conducted in the Laboratory for Mineral Deposits Research (LMDR) at the University of Maryland have shown chalcophile elements such copper, gold, and silver preferentially partition into pyrrhotite under magmatic conditions (Jugo, 1999; Simon, 2003; Tattich, 2012). If pyrrhotite can incorporate indium into its structure as it incorporates other chalcophile elements, then indium could behave as a compatible element. The resultant sequestration of indium by fractional crystallization could then deplete successive melt fractions in indium, and preclude the partitioning of a significant proportion of the original indium budget

of the magma into an exsolving, chloride-bearing MVP. This would lower significantly the probability of forming an indium-bearing ore deposit. Note, however, that even if indium is sequestered in pyrrhotite, the pyrrhotite remains in the magma; there is a possibility that the ore metals sequestered may be released due to the instability of pyrrhotite at certain oxygen and sulfur fugacities (Jugo 1997; Keith et al., 1991; Richards, 1991). Figure 2 shows the stability field of pyrrhotite relative to other minerals in the Fe-S-Si-O system, in log fS_2 - fO_2 space. A change in the sulfur or oxygen fugacity can in essence turn on or off the crystallization of pyrrhotite.

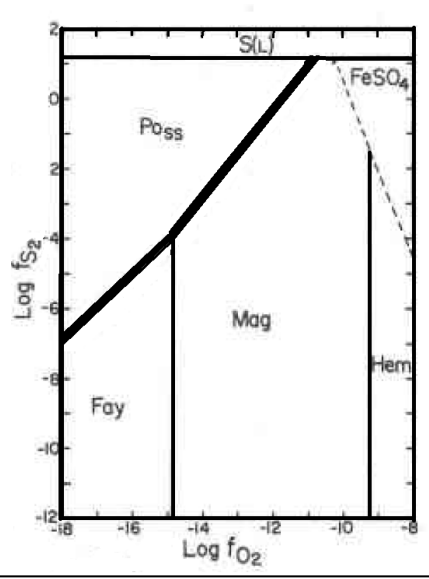


Figure 2. Plot of $\log fO_2$ (oxygen fugacity) versus $\log fS_2$ (sulfur fugacity) for the system Fe-O₂-S₂-SiO₂ (Whitney, 1984). Pyrrhotite stability is restricted to the high fS_2 and $\log fO_2$ systems.

Indium Deposits

The primary sources for indium include massive sulfide deposits, skarn-type deposits, and vein and dissemination deposits (Ishihara et al., 2006). Indium mineralization is closely related to elevated base metal concentrations of tin, zinc, and copper. The indium mineralization in both skarn-type deposits and vein and dissemination deposits is thought to be the result of magmatic-hydrothermal processes.

The Toyoha deposit (Japan) is considered to be one of the largest lead-zinc-copper-silver-indium vein-type deposits in the world. The deposit is hosted by Tertiary sediments, andesite, basalt, and rhyolite (Ohta, 1991). Cross cutting relationships between various veins are consistent with two major mineralization stages (Schwarz-Schampera and Herzig, 2002). The early stage of mineralization is characterized by pyrite-sphalerite-galena in a quartz matrix. The concentration of indium is low to not detectable in the early stage of mineralization (Schwarz-Schampera and Herzig, 2002). The later stage of mineralization is characterized by a high abundance of sulfide minerals. This later stage has been broken up into five substages in which the indium is present in the second, third and fifth substages of mineralization. The later stage veins are considered to have been formed by episodic mineralization with peak temperatures that are 50 to 100° C higher than the estimated maximum formation temperature of the Toyoha

deposit (Schwarz-Schampera and Herzig, 2002). The indium enrichment in these substages is thought to be related to the high temperature mineralization (Ohta, 1991). The total indium content of the Toyoha mine is estimated to be 4,653 tons with an average indium grade of 140 g/t (Ishihara, et al., 2006).

The Mount Pleasant deposit located in New Brunswick, Canada is a granite related veinstockwork tin-tungsten deposit. The indium deposits occur as sulfide-rich veins, breccias, and replacement zones in both granitic rocks and associated volcanic and sedimentary rocks (Sinclair et al., 2006). The most abundant ore minerals associated with the deposit include sphalerite, chalcopyrite, arsenopyrite and cassiterite. The indium grade of the Upper Deep Tin zone, one of the most significant deposits, is 280 g/t. The indium deposits at Mount Pleasant are associated with two distinct episodes of mineralization. The first episode is characterized by low sulfide content (less than 1% by volume) and mineralization from extensive fracture and breccia zones (Sinclair et al., 2006). The granite associated with the first episode represents the earliest period of intrusion by the magma. The second episode of mineralization is more restricted veins and replacement zones and consists of deposits that are moderately to heavily dispersed with sulfides. The change in the structural style of mineralization from extensive fracture and breccia zones to more restricted veins and replacement zones is interpreted by Sinclair et al. (2006) to be caused by decreased volatile pressures that accompanied degassing of the associated granitic magmas. The differences in composition of the related deposits reflect changes in the ore-forming fluids related to the two episodes of mineralization. The Deposition of the indium-bearing sulfide assemblages likely occurred in response to interaction of magmatic-hydrothermal ore-bearing fluids and local ground water (Sinclair et al., 2006). The indium content of the Mount Pleasant deposit is considered one of the highest in the world. The indium grade of the Upper Deep Tin zone, one of the most significant deposits at Mount Pleasant, is 280 g/t (Sinclair et al., 2006).

Partition Coefficients

Partition coefficients are used to model the behavior of trace elements in magmatic-hydrothermal systems. As crystals form in a melt there is a competition at the surface of the crystal among ions of the melt for a position in the crystal's lattice. Ions that are similar in charge, ionic radii, and electronegativity relative to the essential structural constituents of the mineral can potentially be accepted into the crystal structure. If the crystal is in equilibrium with the melt, each component will partition between solid and liquid in such a way that satisfies the condition of equilibrium (McIntire, 1963). The equation that is used to describe the partitioning of trace elements between coexisting phases is the Berthelot-Nernst equation. This states that at equilibrium, the ratio of the concentration of the trace component in the solid to its concentration in the liquid is constant: $D_i = \frac{C_i^{Solid}}{C_i^{liquid}}$ where: C_i^{Solid} and C_i^{Liquid} are the concentration of element i in the solid and liquid respectively. The partition coefficient can be a function of pressure, furgicity or activity of a various components, and temperature but not the concentration of the

fugacity or activity of a various components, and temperature but not the concentration of the trace element. This neglects many thermodynamic effects; however, under restricted conditions, the partition coefficient can be considered as a constant for some calculations. A change in the composition of the melt or its structure can potentially affect the partition coefficient.

Trace elements that are more concentrated in the melt in comparison to the solid crystalline phase will have partition coefficients less than 1 and are referred to as incompatible trace elements. Trace elements with partition coefficients greater than 1 are known as

compatible trace elements and are more concentrated in the crystalline phase. To better understand the evolution of an element in a magma, the bulk partition coefficient (\overline{D}_i) is can be used. The bulk partition coefficient is defined as: $\overline{D}_i = \sum X_i D_i^{\frac{solid}{melt}}$ where: X_i is the weight fraction of mineral i in the products of crystallization and $D_i^{\frac{solid}{melt}}$ is the partition coefficient for the trace element in mineral i.

In an effort to determine if pyrrhotite is important in removing indium from a crystallizing felsic melt, bulk partition coefficients can be used. Audetat and Pettke (2006) modeled the evolution of a porphyry copper-mineralized magma system. In their model they cite the wt% of sulfur in the magma to be 0.13 wt % based on experimental data of Luhr (1990) and S contents of shoshonitic melt inclusions reported by Metrich & Clocciatti (1996). Because pyrrhotite is observed to be the dominant sulfur-bearing phase at magmatic condition, if all of this sulfur was incorporated into pyrrhotite, then the magma would crystallize ~ 0.34 wt% pyrrhotite. For the bulk partition coefficient for indium equal to 1 (that is, indium is neither compatible nor incompatible) then the pyrrhotite/melt partition coefficient for indium would be ~ 290. For indium to be a compatible element the partition coefficient of indium between a silicate melt and pyrrhotite would be greater than 290 and if less than 290 indium would be an incompatible element. Following this rationale, Figure 3 shows the critical relationship between the pyrrhotite/melt partition coefficient for indium vs. weight fraction of pyrrhotite, that yields a bulk partition coefficient equal to 1.

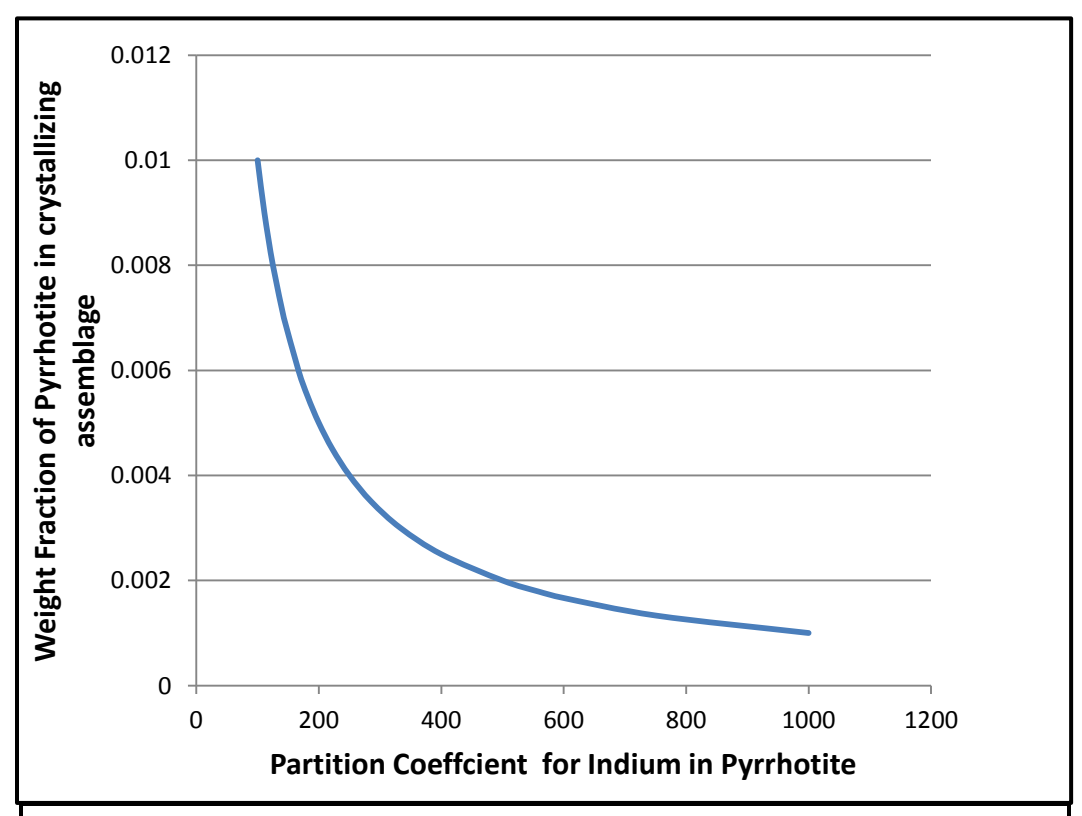


Figure 3. Calculated pyrrhotite/liquid partition coefficients for indium plotted against weight fraction of pyrrhotite that yields a bulk partition coefficient equal to one.

Objectives

Hypothesis

As discussed the demand for indium has increased three fold from 1990 to 2005. Schwarz-Schampera and Herzig, 2002 state "The...behavior of indium during magmatic fractionation processes remains unclear and to a certain degree obscure." Yi et al., 1995 also state "The processes that enrich hydrothermal fluids in indium and tin or remove them prior to sulfide deposition need to be understood." The objective of this study is to determine the partitioning of indium between pyrrhotite and a silicate melt in order to gain an understanding of how pyrrhotite can affect the concentration of indium in the silicate melt. I hypothesize that, in a pyrrhotite-saturated silicate melt, indium will behave as a compatible element due to the effect of pyrrhotite alone.

Test of Hypothesis

To test my hypothesis, experiments were performed with synthetic rhyolite, synthetic pyrrhotite, and indium-gold alloy as the solid phases, and an aqueous solution. Experiments were performed in gold capsules at 100 MPa and 800° C, and for durations of 5 to 15 days. Electron probe microanalysis (EMPA) was used to measure the concentration of indium in the pyrrhotite and the glass, and partition coefficients were calculated. Further experiments were carried out to which either a 1.01 M Σ Cl (0.5 M NaCl; 0.5 M KCl; 0.01M HCl) or a 0.07 M Σ Cl (0.35 M NaCl; 0.35 M KCl; 0.007M CuCl₂) aqueous solution was added. The addition of the former chloride solution potentially allows for indium chloride complexes to form as well as alter the composition of the melt. The latter chloride solution potentially allows for indium chloride complexes to form while at the same time allows the addition of copper to the pyrrhotite structure. The addition of chloride solution as well as copper into the pyrrhotite structure could potentially change the partition coefficient for indium between the pyrrhotite and silicate melt.

Experimental Procedures

Starting Materials

Experimental charges are created using a gold capsule (~17 mm long; 5 mm OD) filled with a synthetic rhyolitic glass, pyrrhotite, indium-gold alloy, and either distilled water,1.01 M Σ Cl (0.5 M NaCl; 0.5 M KCl; 0.01M HCl) or 0.07 M Σ Cl (0.35 M NaCl; 0.35 M KCl; 0.007M CuCl₂) aqueous solution. The pyrrhotite used was synthetically manufactured in the lab and then analyzed by using an EMPA to evaluate the composition and purity. Analysis of the pyrrhotite yielded a composition of Fe $_{(0.832\pm0.004)}$ S (1 σ). The synthetic rhyolite glass was prepared from the components NaAlSi₃O₈, KAlSi₃O₈, and SiO₂, at the USGS, Reston (Simon et al., 2003; Englander, 2005; Table 1).

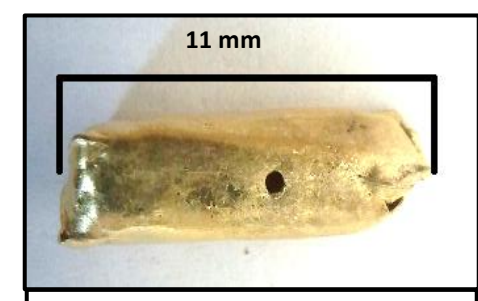


Figure 4. Experimental gold capsule with hole in near center created from indium alloying with the gold capsule during experiment

In the initial experiments, indium was added to the experiments as a pure metal. Those experiments failed: indium metal was found to alloy with the outer gold capsule creating a hole and thus making the experiment useless (figure 4). To prevent the indium from alloying, an indium-gold alloy consisting of 5 wt% indium and 95 wt% gold was synthesized. The alloy (In₅Au₉₅) was synthesized by sealing 5 wt% indium (99.99% pure) and 95 wt% gold (99.99% pure) in a vacuum evacuated, silica tube (fused quartz). The silica tube was inserted into a furnace at 1,070° C for 1 hour, and then submerged into a water bath at room temperature. EPMA of the indium-gold alloy yielded 94.33 \pm 0.30 (1 σ) wt% gold and 5.68 \pm 0.30 (1 σ) wt% indium.

Experimental Design

Gold tubing with 5 mm outer diameter, 0.13 mm wall thickness, and an average length of 18 cm were the starting dimensions of each outer gold capsule. One end of the tube was tricrimped and welded shut using a carbon arc welder. The welded end of the outer capsule was inspected to ensure the weld joints were free of defects. Outer gold capsules were cleaned with a 1 M HCl solution and allowed to dry.

The synthetic rhyolitic glass (30 mg) was loaded into the outer gold capsule first. Two inner gold capsules were created from gold tubing with a 4 mm external diameter, 0.13 mm wall thickness, and a length of approximately 2-3 mm. One end of the inner gold capsule was crimped but not welded while the other end remained open. One of the inner gold capsules held the pyrrhotite (10 mg) and the other held the indium-gold alloy (100 mg). In later experiments the amount of synthetic pyrrhotite added to the inner gold capsule was increased to 30 mg due to the pyrrhotite being hard to analyze. The inner gold capsules prevented the pyrrhotite and indium-gold alloy from physically touching the silicate melt during run conditions but allowed them to still chemically react and reach equilibrium. The small inner gold capsule containing the indium-gold alloy was loaded into the outer gold capsule after the synthetic rhyolitic glass and the pyrrhotite bearing capsule loaded atop. The distilled water or 1.01 M aqueous solution (25 μ L) was loaded into the outer gold capsule via electronic pipette.

Once the starting materials were loaded, the top of the outer gold capsule was tri-crimped and welded shut. To avoid loss due to evaporation of the aqueous solution during welding, the capsule was surrounded by dry ice and a high salinity solution. When the high salinity solution surrounding the capsule freezes it is assumed the experimental aqueous solution inside the capsule is frozen as well. The loss of aqueous solution was evaluated by measuring the mass before welding and after. If the mass of the gold capsule after welding was within ± 0.1 mg of the mass before welding, the capsule was considered good to run.

Sealed capsules were inserted into a René 41 cold seal pressure vessel. The René 41 vessel is composed of a nickel based alloy. A Type-K (Chromel-Alumel) external thermocouple was attached to the vessel to monitor the temperature of the vessel during run conditions. The vessel was inserted into a tube furnace where it was externally heated by doubly-wound Kanthal windings. Pressure was generated by an air pressure-driven water pump. The system was pressurized and heated to 100 MPa and 800° C. Stable run conditions were usually attained within 1 hour after the system reaches 100 MPa and 800°C. The time it took to reach stable run conditions varied due to some furnaces were more efficient at reaching run conditions than others.

Experiments were quenched once the designated run time was reached. The vessel was removed from the furnace and cool compressed air was blown across the vessel until room temperature was reached. The total time to cool the system from 800° C to less than 100° C was under five minutes. The capsule was removed from the vessel and inspected for any holes, cracks, or indications that the integrity of the capsule was altered. The experiment was deemed unsuccessful if there was a weight loss or gain of 1 mg or more. Jugo et al (1999) noted that in similar sulfide bearing experiments that if the capsule failed during run conditions the sulfides would be transformed to magnetite in less than one day. Therefore capsules that had significant weight loss or gain and showed little alteration of the sulfides to magnetite were deemed successful.

Controls

Temperature of the experiment was monitored by using Type-K (Chromel-Alumel) external thermocouples. Thermal gradients in the furnace were evaluated previously by Dr. Brian Tattich. By using a series of internal thermocouples, he determined a thermal gradient of approximately 4° C across the length of a sample capsule, and recorded temperatures within 1 to 2°C to an external Type-K external thermocouple. The furnace was inclined 12° with the hot end up to minimize convection at the hot end of the vessel (Frank, 2001; Englander, 2005; Tattich, 2012). The René vessels and furnaces used in this study are the same as those used by Tattich (2012).

Pressure in the experiments was generated by a compressed air-driven water pump as well as the pressure increase due to the heating of the water used to pressurize the vessel. Pressure was monitored using Bourdon tube gauges calibrated against a factory-calibrated Heise gauge. Small adjustments in pressure were made by slowly leaking water out of the pressure system. Precision of pressure measurements was obtained by recording the change in pressure at the same time twice a day over five days and calculating the standard deviation. Pressure measurements are precise to \pm 0.5 MPa.

Oxygen fugacity was controlled by the composition of the René 41 vessel. Since the vessel is made primarily from nickel, the equilibrium between nickel and nickel-oxide controlled the oxygen fugacity once a layer of nickel oxide formed. Equation 1 shows the reaction between the nickel and the water inside the vessel generating nickel oxide and hydrogen. The hydrogen gas produced from the creation of nickel oxide is capable of diffusing in and out of the gold capsule. The oxygen fugacity of the Rene vessels is only applicable if the hydrogen reaches osmotic equilibrium through the capsule's wall (Jugo, 1997). Hydrogen diffusion through gold capsules usually requires between 7 and 25 hours (Tattich et al., 2009). In order to characterize the oxygen fugacity of the vessels at 800° C and 100 MPa, oxygen sensor experiments were conducted by Dr. Brian Tattich using Co-Pd alloys. An intrinsic log oxygen fugacity ($\log f_{02}$) value of -13.72 ± 0.4 was used in this study.

$$Ni + H_2O \rightarrow NiO + H_{2(g)}$$
 Equation (1)

Sulfur fugacity in the experiments was calculated based on the run product pyrrhotite composition using the method of Toulmin and Barton (1964):

$$log f_{S_2} = (70.03 - 85.83N) \left(\frac{1000}{T} - 1 \right) + 39.30(1 - 0.9981N)^{1/2} - 11.91$$

where T is temperature in Kelvin, N is the mole fraction of pyrrhotite in the system FeS-S₂, and is defined as: $N = 2\left(\frac{nFe}{nFe+nS}\right)$. For experiments containing copper in the pyrrhotite the sulfur fugacity was calculated using the method of Mengason et al., 2010 where $N = 2\left(\frac{nFe+nCu}{nFe + 1.5nCu + nS}\right)$

Demonstration of Equilibrium

Equilibrium will be demonstrated through time invariance. Time invariance is shown by running experiments with varying times and with increasing duration of the experiments, the partition coefficient either approaches or scatters about a mean. Two other cases are possible for time invariance. The first case indicates there is no change in the starting materials. This case is discarded due to a difference in the initial phases in comparison to the final phases. The second case is for steady states system in which there is continuous input and output of mass. The experimental setup is closed also discarding this case. For the kind of experiments performed in this study, time invariance is required and adequate condition for demonstrating equilibrium.

Oxide	wt %
SiO ₂	80.4 ± 1.4
K ₂ O	4.67 ± 0.43
CaO	0.02 ± 0.01
Na ₂ O	3.58 ± 0.24
Al_2O_3	10.9 ± 1.1
FeO	bd
Cl	0.05 ± 0.05
Total	99.6 ± 0.9
ASI	0.99

Table 1. Synthetic rhyolite (GR-1) used in experiments. All concentrations are reported in weight percent oxide, with the exception of Cl, and are reported with a 1σ standard deviation (Englander, 2005; Simon et al., 2003). bd indicates that the FeO concentration is below detection.

Analytical Techniques

Binocular Microscope

A binocular microscope with a separate light source was used to inspect the run products. The outside of the gold capsule was inspected to determine if the integrity of the gold capsule has been compromised. A standard razor blade was used to open the gold capsule. Run products were inspected to identify the mineral phases present as well as inspect the glass for homogeneity.

Electron Probe Microanalyzer

A JEOL JXA-8900 electron probe microanalyzer was used to determine major and minor element concentrations in the glass and pyrrhotite run products. Major elements include Si, Al, Fe, Na, Ca, K, and Cl. The minor elements include indium and Cu. Wavelength dispersive spectroscopy (WDS) was used to determine major and minor element concentrations. Energy dispersive spectrometry (EDS) can provide semi-quantitative analysis of the run products prior to WDS, and was used in some cases for phase identification. Standards with known concentrations of major and minor elements was used to determine the accuracy of EPMA results.

The glass from each of the successful experiments was mounted in Buehler© EpoFix casting epoxy and polished. Diamond paste of varying grit sizes ($15\mu m$ to $1\mu m$) was used to polish the mounted glasses. Once polished, the epoxy mounts was coated with a layer of carbon ($200\text{-}300\ \text{Å}$) using a thermal evaporator, to avoid charge build up on the samples.

Analyses are performed in two steps: the glasses are analyzed for major and minor elements; and subsequently followed by the analysis for indium. The major elements were analyzed first due to the possibility of alteration in the glass caused by the higher accelerating voltage and cup currents used to analyze the concentration of indium in the glass. Sodium and potassium diffused due to the heating of the sample during the high currents necessary for the indium analyses. Major elements were analyzed with a 15kV accelerating voltage, 2.5 nA cup current and a beam diameter of 20-30 μ m. K α characteristic X-rays lines were used to identify the major elements. Natural rhyolite from Yellowstone was used as a standard for Si, K, Fe, Al and Ca. Scapolite was used as a standard for Cl and S and rhodonite was used as a standard for Mn. In the case of indium in the run product glasses, the uncertainty due to counting statistics was 1.6% at 500 ppm indium level.

Indium was analyzed in the glass with a 20 kV accelerating voltage, 200 nA cup current and a beam diameter of 1 μ m. L β characteristic X-rays lines were used in the analysis of indium. La characteristic x-ray lines were not used due to the potential overlap with the potassium Ka x-ray line. NBS 610 is used as a standard for indium. The accepted indium concentration in NBS 610 was 439 ppm. As a test of indium accuracy, using the indium arsenide standard and measuring NBS 610 as an unknown, the concentration of indium in NBS 610 was found to be an average of 459 ppm (range: 439-477 ppm, N = 5).

The pyrrhotite from each of the successful experiments was mounted, polished and coated with carbon in the same manner as the glass. Semi-quantitative analysis was performed on pyrrhotite grains using EDS to ensure the run products were not completely altered to magnetite during the experiments. The accelerating voltage for the pyrrhotite analysis was 20

kV with a cup current of 50 nA. Standards used for the analysis of the pyrrhotite were Santa Eulalia pyrrhotite, chalcopyrite and indium arsenide. In the run product pyrrhotite, the uncertainty due to counting statistics is 1.1 relative % at 2000 ppm indium level.

Uncertainty of Analysis

To determine the uncertainty associated with measurements acquired from the EPMA counting statistics were applied. The uncertainty was calculated using the equation 1σ (relative uncertainty) = $\frac{\sqrt{n}}{2}$ where n is equal to the number of x-ray counts measured.

 1σ (relative uncertainity) = $\frac{\sqrt{n}}{n}$ where n is equal to the number of x-ray counts measured. Uncertainty associated with the calculation of the average concentration of indium in the run products was calculated by first calculating the arithmetic mean of the concentrations and then calculating the standard deviation of the concentrations. The standard deviation was calculated using the equation: $\sqrt{\frac{\sum (x-\bar{x})^2}{(n-1)}}$ where x is equal to each measured concentration, \bar{x} is equal to the arithmetic mean of the concentrations and n is equal to the number of analysis performed. Propagation of uncertainty for a ratio was used to calculate the uncertainty associated with calculating the partition coefficient for each experiment. The equation used to propagate uncertainty for a ratio is:

 $R = \frac{N}{D} \frac{\epsilon(R)}{R} = \sqrt{\left(\frac{\epsilon(N)}{N}\right)^2 + \left(\frac{\epsilon(D)}{D}\right)^2}$ where: R is equal to the ratio, N is the numerator, D is the denominator, $\epsilon(R)$ is the uncertainty associated with R, $\epsilon(N)$ is the uncertainty associated with N, $\epsilon(D)$ is the uncertainty associated with D.

Experimental Results

Partition Coefficient for Indium Between Pyrrhotite and Silicate Melt

Fourteen experiments were considered successful and the run products were analyzed by EPMA. The initial compositions of these charges, duration of the experiments, and weight loss for each capsule are summarized in Table 2; bulk composition of the resulting glasses including Cl and S concentrations are given in Table 3. A Nernst-type partition coefficient for indium between pyrrhotite and silicate melt was calculated by using the concentrations of indium in

pyrrhotite and silicate melt (Table 4). Figure 5 shows three separate plots of $D_{In}^{\frac{Po}{melt}}$ vs. experimental duration for pure water, chloride-bearing, and copper-bearing experiments. These

plots generally show that the $D_{In}^{\frac{Po}{melt}}$ approaches equilibrium with increasing run duration, with the partition coefficient either approaching or scattering about a mean.

Five day duration experiments that contained pure water as the aqueous solution had a concentration ($\pm 1\sigma$) of indium in pyrrhotite ranging from 0.16 (\pm 0.03) wt% to 0.29 (\pm 0.06) wt% and a concentration of indium in the melt ranging from 0.0056 (\pm 0.0016) wt% to 0.044 (\pm

0.001) wt%. The $D_{In}^{\frac{Po}{melt}}$ for five day experiments ranged from 6.43 (±1.4) to 28.34 (± 10.0). Longer duration experiments (10 days) that demonstrate an approach toward equilibrium had a concentration of indium in pyrrhotite ranging from 0.18 (±0.02) wt% to 0.29 (±0.04) wt% and a concentration of indium in the melt ranging from 0.015 (±0.005) wt% to 0.032 (±0.012) wt%.

Table 2. Summary of Experimental Conditions All experiments at $800^{\circ}\ C$ and $100\ MPa$

Run	Star	ting material (m	g)	Aq	Capsule V	Veight (g)	ΔW (mg)	Duration
Kuli	Po	In-Au alloy	Glass	(µL)	Initial (W _o)	Final (W _f)	(W_f-W_o)	seconds x 10 ⁵ (days)
104	10.7	5.2*	29.9	22	1.02867	1.02858	-0.9	4.3 (5 days)
105	10.1	100.1	30.1	25	1.18334	1.18329	-0.5	4.3 (5 days)
120	25.5	101.2	30.4	25	1.18845	1.18838	-0.7	8.6 (10 days)
122	25.2	101.1	30.4	25	1.23173	1.23159	-1.4	8.6 (10 days)
107	11.3	101.9	29.6	25	1.11429	1.11422	-0.7	4.3 (5 days)
110	10.2	100.5	30.0	25	1.10424	1.10420	-0.4	4.3 (5 days)
109	11.0	103.0	30.3	25	1.12804	1.12798	-0.5	13.0 (15 days)
113	10.1	99.4	30.1	25	1.03752	1.03744	-0.8	13.0 (15 days)
115	25.6	100.7	30.1	25	1.17833	1.17713	-1.2	4.3 (5 days)
116	25.8	101.4	30.5	25	1.17123	1.17023	-1.0	4.3 (5 days)
117	25.6	101.6	30.2	25	1.17331	1.17328	-0.3	8.6 (10 days)
118	25.3	100.0	30.1	25	1.22753	1.22744	-0.9	8.6 (10 days)
119	25.7	101.6	30.5	25	1.23405	1.23396	-0.9	13.0 (15 days)
121	20.1	101.3	30.5	25	1.29885	1.29877	-0.8	13.0 (15 days)

Note: uncertainties in mass are 0.0001g (0.1 mg). * Amount of pure indium added

Table 3. Analyses of major elements for glass run products (wt%).

Run	SiO ₂	Al ₂ O ₃	Na ₂ O	K ₂ O	CaO	FeO	MgO	SO ₃	Cl	Total	ASI
104	75.94 ± 1.35	10.79 ± 0.42	3.58 ± 0.66	4.01 ± 0.13	bd	0.54 ± 0.32	bd	bd	0.01 ± 0.001	94.84 ± 1.25	1.06 ± 0.12
105	74.52 ± 1.59	11.47 ± 0.98	3.07 ± 0.52	4.34 ± 0.35	bd	bd	0.08 ± 0.08	bd	0.03 ± .001	93.53 ± 0.32	1.18 ± 0.09
120	75.96 ± 0.45	11.06 ± 0.31	3.95 ± 0.18	4.24 ± 0.18	bd	bd	bd	bd	0.01 ± 0.001	95.36 ± 0.012	1.00 ± 0.02
122	75.48 ± 1.04	11.25 ± 0.44	4.05 ± 0.19	4.42 ± 0.13	bd	bd	bd	bd	0.015 ± 0.0046	95.31 ± 0.76	0.98 ± 0.01
107	75.58 ± 3.26	10.60 ± 0.52	4.22 ± 0.02	4.99 ± 0.05	bd	0.55 ± 0.04	bd	0.05 ± 0.00	0.36 ± 0.26	96.56 ± 3.23	0.86 ± 0.04
110	73.98 ± 1.10	11.34 ± 0.54	4.53 ± 0.54	5.20 ± 0.20	0.04 ± 0.02	0.42 ± 0.34	bd	bd	0.18 ± 0.04	95.73 ± 0.81	0.86 ± 0.03
109	74.55 ± 0.57	10.20 ± 0.39	3.65 ± 0.53	4.79 ± 0.22	bd	1.16 ± 0.10	bd	bd	0.18 ± 0.04	96.64 ± 1.16	0.92 ± 0.07
113	74.48 ± 0.93	10.89 ± 0.46	4.46 ± 0.27	5.05 ± 0.21	0.03 ± 0.01	0.83 ± 0.20	bd	bd	0.19 ± 0.02	95.92 ± 0.80	0.85 ± 0.02
115	74.20 ± 0.41	11.06 ± 0.48	3.77 ± 0.26	5.04 ± 0.15	bd	0.77 ± 0.06	bd	0.04 ± 0.02	0.16 ± 0.01	95.13 ± 0.63	0.95 ± 0.03
116	73.88 ± 1.13	10.23 ± 0.26	3.91 ± 0.11	5.02 ± 0.05	bd	1.62 ± 0.08	bd	bd	0.31 ± 0.01	95.12 ± 0.70	0.86 ± 0.00
117	74.84 ± 0.70	10.43 ± 0.34	3.45 ± 0.13	4.76 ± 0.15	0.01	0.62 ± 0.07	bd	bd	0.02 ± 0.02	94.22 ± 0.43	0.96 ± 0.02
118	73.91 ± 0.003	10.69 ± 0.56	4.04 ± 0.18	4.93 ± 0.27	bd	0.74 ± 0.01	bd	bd	0.27 ± 0.01	94.67 ± 0.98	0.89 ± 0.002
119	74.49 ± 1.23	10.94 ± 0.37	3.91 ± 0.16	5.04 ± 0.13	bd	0.93 ± 0.53	bd	bd	0.19 ± 0.02	95.59 ± 0.74	0.92 ± 0.03
121	75.84 ± 0.44	11.07 ± 0.34	3.61 ± 0.10	4.89 ± 0.11	bd	0.28 ± 0.07	bd	0.05 ± 0.02	0.13 ± 0.01	95.95 ± 0.27	0.98 ± 0.01

Uncertainties are presented as the standard deviation from the mean (1σ) bd = value below detection.

The $D_{ln}^{\frac{Po}{melt}}$ for 10 day, pure water experiments ranged from 9.32 (± 3.9) to 12.05 (± 4.1). This yields and average $D_{ln}^{\frac{Po}{melt}} \approx 10$ for experiments run with pure water. There are two possible

reasons why pure water yielded the highest $D_{In}^{\frac{Po}{melt}}$. First, without chlorine to stabilize indium in the melt, these experiments exhibited the lowest concentrations of indium in the melt for a given

concentration of indium in pyrrhotite. Secondly, a higher $D_{In}^{\frac{Po}{melt}}$ may result from the effect of the Aluminum Saturation Index (ASI). Further discussions of indium stabilization in the melt as well as ASI are found in the following section.

Experiments containing a 1.01 M chloride solution yielded, for 5 day experiments, concentrations ($\pm 1\sigma$) of indium in pyrrhotite ranging from 0.14 (± 0.03) wt% to 0.22 (± 0.10) wt% and a concentration of indium in the melt ranging from 0.048 (± 0.03) wt% to 0.049 wt%.

Five day experiments generated a $D_{In}^{\frac{Po}{melt}}$ between 2.97 (± 1.4) and 4.42 (± 2.4). Experiments carried out for a duration of 15 days had a concentration of indium in pyrrhotite ranging from 0.05 ± 0.01) wt% to 0.16 ± 0.05) wt% and a concentration of indium in the melt ranging from $0.056 (\pm 0.006)$ wt% to $0.076 (\pm 0.01)$ wt%. As equilibrium is approached for 15 day chloride-

bearing experiments $D_{ln}^{\frac{Po}{melt}}$ converged on the interval 0.91 (± 0.18) to 2.14 (±0.83). The average $D_{ln}^{\frac{Po}{melt}} \approx 1.5$. The $D_{ln}^{\frac{Po}{melt}}$ decreases for chloride-bearing experiments as a result indium being stabilized in the silicate melts. Indium stabilization in the melt is an effect of the addition of chlorine to the melt. The presence of chlorine in the melt also increases the stability of iron in the melt. Iron is able to form complexes with chlorine-forming FeCl₂. The presence of chlorine and iron in the melt allows for indium-iron-chlorine complexes to form in the melt thus stabilizing indium in the melt and increasing the concentration of indium

Experiments that contained a 0.35 M CuCl₂-bearing aqueous solution yielded the largest concentration of indium in pyrrhotite. The concentration of indium in pyrrhotite for 5 day CuCl₂ bearing experiments ranged from $0.14 (\pm 0.03)$ wt% to $0.23 (\pm 0.08)$ wt% and a concentration of indium in the melt ranged from $0.068 (\pm 0.008)$ wt% to $0.074 (\pm 0.002)$ wt%. With longer experimental duration (15 days) the concentration of indium in pyrrhotite ranged from 0.021 (± 0.003) wt% to 0.18 (\pm 0.03) wt% and a concentration of indium in the melt ranged from 0.020 (\pm

0.002) wt% to 0.039 (± 0.002) wt%. The $D_{ln}^{\frac{Po}{melt}}$ for 5 day experiments was between 2.01 (± 0.57)

and 3.11 (± 1.0) and for 15 day experiments the $D_{In}^{\frac{Po}{melt}}$ was between 1.09 (±0.16) and 4.54

(±0.87). Copper-bearing experiments yield an average $D_{In}^{\frac{Po}{melt}} \approx 3$. The increase in the concentration of indium in pyrrhotite for the CuCl₂-bearing experiments could be attributed to the ability for indium to pair with copper through coupled substitution. Equation 2 demonstrates how copper present as CuCl₂ can enter the pyrrhotite structure. Once copper is present in the pyrrhotite structure, indium has the capability of substituting for iron in the pyrrhotite yielding the roquesite component of pyrrhotite. Equation 3 demonstrates this reaction.

$$HCl + CuCl_2 + 2FeS^{Po} = CuFeS_2^{Po} + FeCl_2 + \frac{1}{2}H_2$$
 Equation 2

$$\frac{1}{2}H_2 + CuFeS_2^{Po} + InCl_3 = CuInS_2^{Po} + FeCl_2 + HCl$$
 Equation 3

If each individual factor is isolated my analysis suggests that an increase in chlorine in the system will cause the $D_{In}^{\frac{Po}{melt}}$ to decrease. Although the $D_{In}^{\frac{Po}{melt}}$ does vary depending upon the aqueous solution the combination of these data sets indicates that the best estimate for the partition coefficient for indium between pyrrhotite and silicate melt is on the order of 4.

Aluminum Saturation Index

The aluminum saturation index (ASI) is a measure of the melts aluminosity and is defined as the molar ratio: $[Al_2O_3/(CaO+K2O+Na_2O)].$ ASI greater than 1 indicates that the melts has excess aluminum in relation to alkalis. Table 3 shows the ASI for the fourteen successful experiments. The ASI for the starting glass was 0.99 (Tattich 2012) (Table 1). Experiments that contained only pure water had an ASI (1 σ) (0.98 (±0.01) and 1.00 (±0.02)) that varied little to none when compared to the starting ASI. The chloride- and copper-bearing glasses indicate that all experimental melts were peralkaline (i.e. ASI < 1 and Al₂O₃<(K₂O+Na₂O). The ASI for chloride-bearing experiments ranged between 0.85 (±0.02) and 0.92 (±0.07). Copper (II) chloride-bearing experiments had and ASI that ranged from 0.92 (±0.03) and 0.98 (±0.01). The starting synthetic glass for pure water experiments did not vary much due to the melt having little interaction with aqueous fluid. Experiments that contained chloride-bearing solutions experienced an increase in concentration of sodium and potassium in the melt due to the mass transfer between the aqueous fluids and the melt. The addition of chlorine

caused the $D_{ln}^{\frac{10}{melt}}$ to drop by a factor of 6; note however the ASI of the melt also drops. This suggests the drop in ASI may also contribute to this effect.

Table 4. Concentration of indium in run products (wt%) and calculated partition coefficient for indium between pyrrhotite and silicate melt. Uncertainty = 1σ

Run	[In] in pyrrhotite Wt % ± 1σ	[In] in glass Wt % ± 1σ	$D_{In}^{\frac{Po}{melt}} \pm 1\sigma$
104	0.29 ± 0.063	0.044 ± 0.002	6.43 ± 1.45
105	0.16 ± 0.03	0.0056 ± 0.0016	28.34 ± 10.09
122	0.18 ± 0.022	0.015 ± 0.005	12.05 ± 4.10
120	0.29 ± 0.05	0.032 ± 0.010	9.32 ± 3.94
107	0.22 ± 0.12	0.049 ± 0.00	4.42 ± 2.41
110	0.14 ± 0.07	0.048 ± 0.03	2.97 ± 1.37
109	0.16 ± 0.05	0.076 ± 0.014	2.14 ± 0.83
113	0.05 ± 0.01	0.056 ± 0.007	0.91 ± 0.18
115	0.14 ± 0.03	0.068 ± 0.01	2.01 ± 0.57
116	0.23 ± 0.08	0.074 ± 0.002	3.11 ± 1.03
117	0.20 ± 0.03	0.047 ± 0.006	4.29 ± 1.04
118	0.31 ± 0.10	0.039 ± 0.002	7.88 ± 2.56
119	0.021 ± 0.003	0.020 ± 0.002	1.09 ± 0.16
121	0.18 ± 0.03	0.039 ± 0.002	4.54 ± 0.87

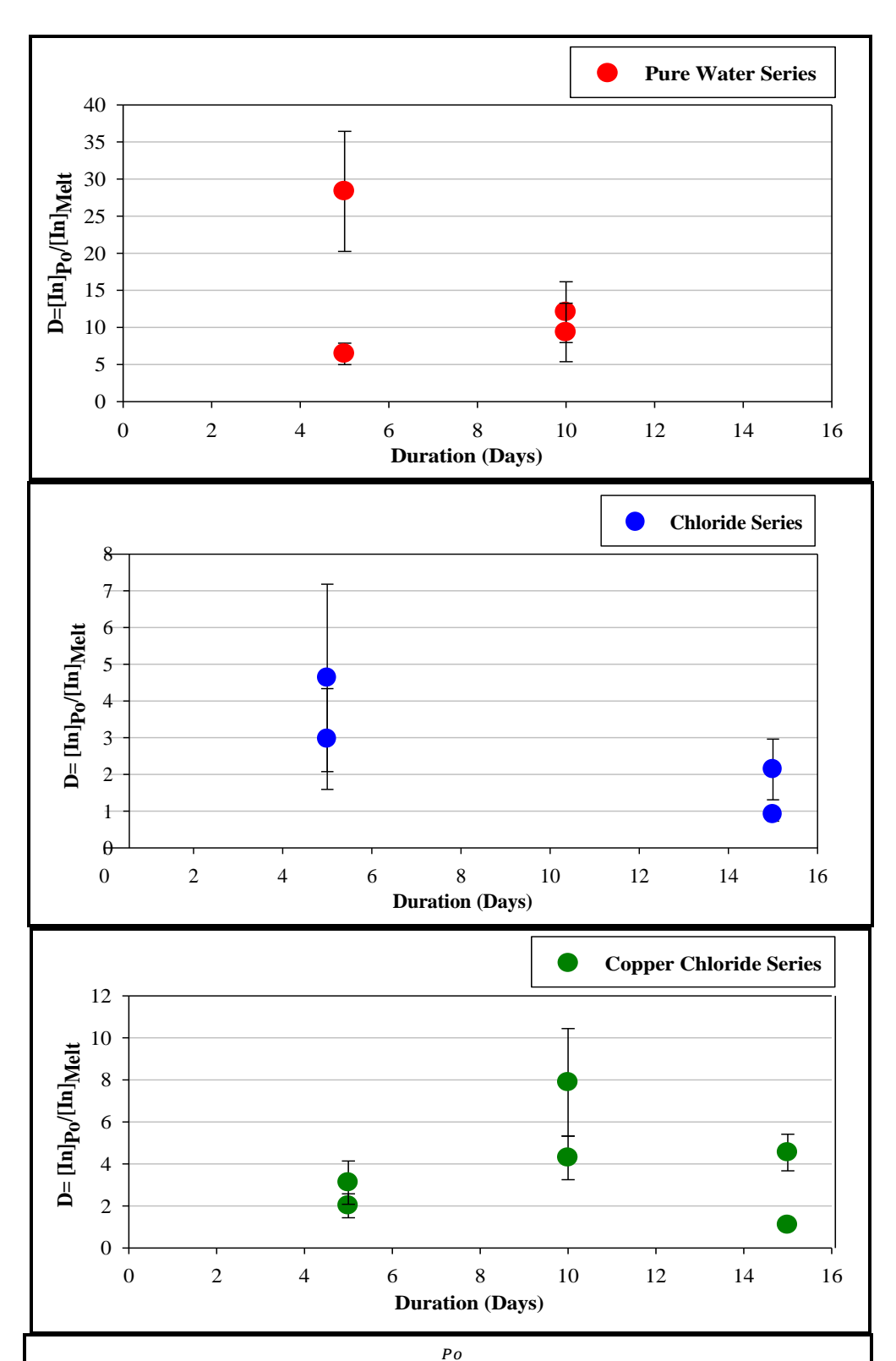


Figure 5. Three separate plots of $D_{In}^{\frac{Po}{melt}}$ vs. experimental duration for pure water, chloride bearing, and copper bearing experiments. These plots demonstrate an approach toward equilibrium. With increasing duration of the experiments, the partition coefficient either approaches or scatters about a mean

Discussion

Indium Sequestration by Pyrrhotite

To better understand and quantify the effect of pyrrhotite on the concentration of indium in a silicate melt a modified form of the Rayleigh fractionation equation was used (Simon et al., 2003).

$$m_{In}^{Melt} = m_{In}^{Melt,intial} \times F^{\overline{D}}$$
 Equation 4

Equation 4 shows the Rayleigh fractionation equation where m is the mass, rather than the concentration, of the indium in melt, F is the fraction of melt remaining and \overline{D} is the bulk partition coefficient for indium between pyrrhotite and silicate melt (i.e., the product of the partition coefficient for indium between pyrrhotite and melt and the mass fraction of pyrrhotite in melt). Although there are other crystalline phases, such as oxides and silicates, into which indium could potentially partition, we are interested specifically in understanding the effect of pyrrhotite alone on sequestration of indium in a silicate melt. This approach is justified given the dominant role played by pyrrhotite in the sequestration of elements such as copper (Lynton et al., 1993; Williams et al., 1995; Simon et al., 2006). The mass fraction of pyrrhotite used to calculate the bulk partition coefficient was varied from 1×10^{-5} to 0.003. Using a partition coefficient of

 D_{In}^{Po} = 4 and the varying mass fractions of pyrrhotite cited above yields a bulk partition coefficient values of \overline{D} = 4 ×10⁻⁵ and 0.012. The fraction of melt remaining will be the amount of melt present at water saturation of a felsic melt that contains 4 wt% water, initial. A granitic magma with 4 wt % water, at 200 MPa, will crystallize one-third before it becomes vapor saturated at approximately 6 wt% water; therefore, F = 0.66. The proportion of indium sequestered by pyrrhotite as a function of *F* is provided in Table 5 and Figure 6. Pyrrhotite sequesters 0.002% indium at \overline{D} = 4 ×10⁻⁵ and 0.5% indium at \overline{D} = 0.012. These results demonstrate that pyrrhotite alone cannot sequester significant indium and negates the hypotheses that indium behaves as a compatible element due to the effect of pyrrhotite alone.

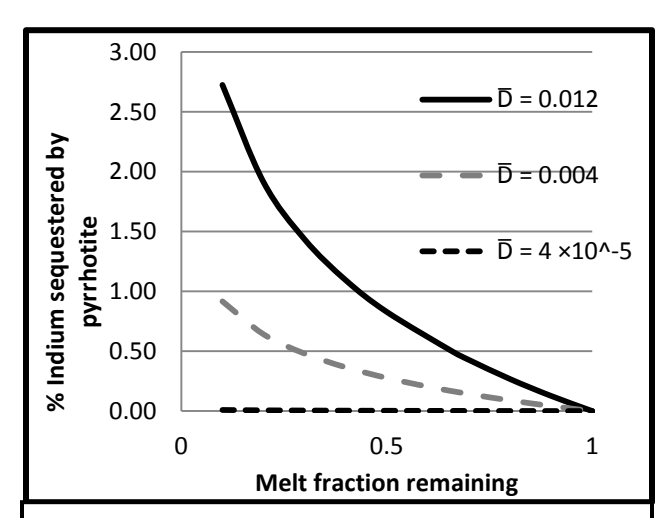


FIGURE 6. The fraction of indium in felsic magma that is sequestered by pyrrhotite, calculated using a partition coefficient value of $\frac{Po}{r}$

 $D_{In}^{\overline{melt}} = 4$ and mass fractions of pyrrhotite in felsic magma of 1×10^{-5} and 0.003.

TABLE 5. The proportion of indium sequestered by pyrrhotite in felsic magma after 30% fractional crystallization

$D_{In}^{rac{Po}{melt}}$	Mass Fraction of Pyrrhotite	\overline{D}	Indium Sequestered by Pyrrhotite %
4	1 ×10 ⁻⁵	4×10 ⁻⁵	0.002
4	0.001	0.004	0.2
4	0.003	0.012	0.5

Other Hypotheses for Indium Sequestration in Magmas

The results of this study demonstrate that pyrrhotite alone is not capable of sequestering indium. This study is one of the initial studies in better understanding the behavior of indium at magmatic conditions. In an effort to further explore the behavior of indium I have designed a model to examine the effects of minerals as whole on the partitioning of indium in varying rock types as well as examine the upper concentration of indium in an evolving ore fluid. This model allows us to place a broad constraint on the indium budget.

Wager et al., (1958) studied the indium concentration in rocks and minerals from the Skaergaard intrusion located in East Greenland. The Skaergaard layered basic intrusion in East Greenland is regarded as a classic example of the extreme differentiation of magma (Hunter et al., 1987). The concentration of indium in the minerals that constitute the hortonolite ferrogabbro was measured by Wager et al., 1958. These minerals include: plagioclase, olivine, pyroxene, magnetite and ilmentite. Wager (1958) made the assumption that the concentration of indium in the melt of the original magma, from which the complex was formed, can be represented by the chilled the marginal gabbro. Table 6 summarizes the concentrations of indium in the minerals and chilled marginal gabbro. Using the concentration of indium in the crystalline phases and the concentration of indium between the crystalline phases and the chilled marginal gabbro. The bulk partition coefficient for indium was also calculated by using the date from Wager et al., 1958. The calculated partition coefficients as well as the bulk partition coefficient are given in Table 6.

Minerals	[In] (ppm)	Proportion of Minerals in Rock (Weight %)	mineral D _{In} melt	$D_{In}^{rac{mineral}{melt}} imes ext{wt } \%$	\overline{D}
Plagioclase	0.0032	54	0.06	0.032	
Olivine	0.056	13	1	0.13	
Pyroxene	0.18	23	3.2	0.74	1.3
Magnetite	0.16	4.5	2.9	0.13	
Ilmenite	0.29	5.5	5.2	0.29	
Chilled Marginal Gabbro	0.056				

Table 6. Partition coefficient and concentration if indium in minerals comprising a hortonolite ferrogabbro of the Skaergaard intrusion, East Greenland. The chilled marginal gabbro is assumed to be the original melt composition. Concentrations and weight % data from Wager et al., 1958.

Using the hypothetical bulk partition coefficient for indium, I modeled the proportion of indium that is sequestered for the hortonolite ferrogabbro by means of the modified Rayleigh fractionation equation (equation 4). The fraction of melt remaining was set at 17% (i.e. F=0.17). This would be the amount of melt present for a melt that has and initial 1wt% water and became water saturated at 6 wt% water. Figure 7 shows the percent indium sequestered as a function of

the melt fraction remaining. With 17% of the melt remaining, approximately 90% of the indium in the melt has been sequestered by the crystalline phases. Of the crystalline phases, indium is predominantly taken out of the melt by the iron-bearing phases (i.e. magnetite, ilmenite, and pyroxene).

To make an upper estimate of the amount of indium available for ore formation, I allow all the indium present in the 17% melt remaining to partition into the water vapor. Thus, if e.g., 90% of the indium originally in the melt is sequestered, then 10 % of the original indium is available to partition in to the water vapor. In the calculations presented herein, the initial concentration of indium in the melt is taken to be the concentration of indium in the chilled marginal gabbro of the Skaergaard intrusion (0.056 ppm). Ten percent of the initial concentration of indium in the melt is 0.0056 ppm, which can also be written as the weight fraction $\frac{0.0056 \ ng \ indium}{1 \ g \ melt}$. As explained above the melt contains 1 wt% water which can be written as a weight fraction $\frac{0.01 \ g \ water}{1 \ g \ melt}$. If all the indium goes into the water vapor then the concentration of indium in the water can be written as the weight fraction $\frac{0.0056 \ ng \ indium}{0.01 \ g \ water}$ which can be written 0.56 ppm. Therefore 10% of the initial concentration is 0.0056 ppm and the concentration of indium in the ore fluid is 0.56 ppm.

Because magnetite and ilmenite are strong candidates for sequestration of indium, I also chose to model the proportion of indium sequestered using the modal compositions of selected Japanese magnetite-ilmenite biotite-hornblende granodiorites from the Tokuwa batholith, Central Japan. These granodiorites represent a well-studied series of rocks in an arc environment where there is significant variation in the magnetite-ilmenite content in the rocks. In this model I set five rules:

- 1. The partition coefficients for indium between the crystalline phases and melt are the same as the partition coefficients for the hortonolite ferrogabbro. The partition coefficients for quartz and alkali feldspar in the granodiorites are the same as plagioclase in the hortonolite ferrogabbro.
- 2. The amount of indium taken up by the ferromagnesian silicates in the hortonolite ferrogabbro (i.e. pyroxene and olivine) is considered lost to ferromagnesian silicates in the granodiorite. The ferromagnesian minerals present in the granodiorite are biotite and hornblende.
- 3. The concentration of indium in the chilled marginal gabbro from the Skaergaard intrusion is used as the concentration of indium in the melt.
- 4. The fraction of melt remaining is set equal to 0.17. This is assumed to be the amount of melt remaining after fractional crystallization of a melt that contained an initial 1wt% water and became water-saturated at 6 wt% water.
- 5. The amount of indium present at water saturation is the maximum amount of indium that can partition into the evolving ore fluid at that time. We ignore the fact that there are still crystals forming in the melt to give an upper limit calculation.

The first type of granodiorite we modeled was a magnetite-rich granodiorite. Table 7 shows the modal abundance of minerals present in the magnetite-rich granodiorite. The bulk partition coefficient for the magnetite-rich granodiorite is equal to 0.67 (Table 7). Applying the modified Rayleigh fractionation equation and using F=0.17 shows that with 17% melt remaining 60% of the indium in the melt will have been sequestered by the crystalline phases. The percent indium

sequestered by the crystalline phases as a function of melt fraction remaining is provided in Figure 7. This leaves approximately 30% of the original indium in the melt to be available to go into the ore fluid. Assuming the initial concentration of indium in the melt to be the concentration of indium in the chilled marginal gabbro from the Skaergaard intrusion (0.056ppm) the amount of indium left in the 17 % melt remaining would be 0.022 ppm. Therefore, the concentration of indium in the ore fluid (i.e. 1wt% water) is 2.2 ppm.

Minerals	Modal Abundance%	[In] (ppm)	Mass Fraction %	$D_{In}^{rac{mineral}{melt}}$	$D_{In}^{\frac{mineral}{melt}} imes rac{Mass}{Fraction}$	D
Plagioclase	38	0.0032	37	0.06	0.02	
Quartz	31	0.0032	29	0.06	0.017	
Alkali Feldspar	18	0.0032	18	0.06	0.011	0.67
Fe-Mg Silicates	12	0.23	14	4.1	0.57	0.07
Magnetite	0.9	0.16	1.6	2.9	0.05	
Ilmenite	0	0.29	0	5.2	0	
Chilled Marginal Gabbro		0.056				

Table 7. Modal abundance of minerals comprising a magnetite-rich hornblende-biotite granodiorite. The chilled marginal gabbro is assumed to be the original melt composition. Concentrations and modal abundance data from Shimizu (1986).

The second type of granodiorite we modeled was an ilmenite-rich granodiorite. Table 8 shows the modal abundance of minerals present in the ilmenite-rich granodiorite. The bulk partition coefficient for the ilmenite-rich granodiorite is equal to 0.18 (Table 8). Applying the modified Rayleigh fractionation equation and setting F=0.17 shows that with 17% melt remaining 24% of the indium in the melt will have been

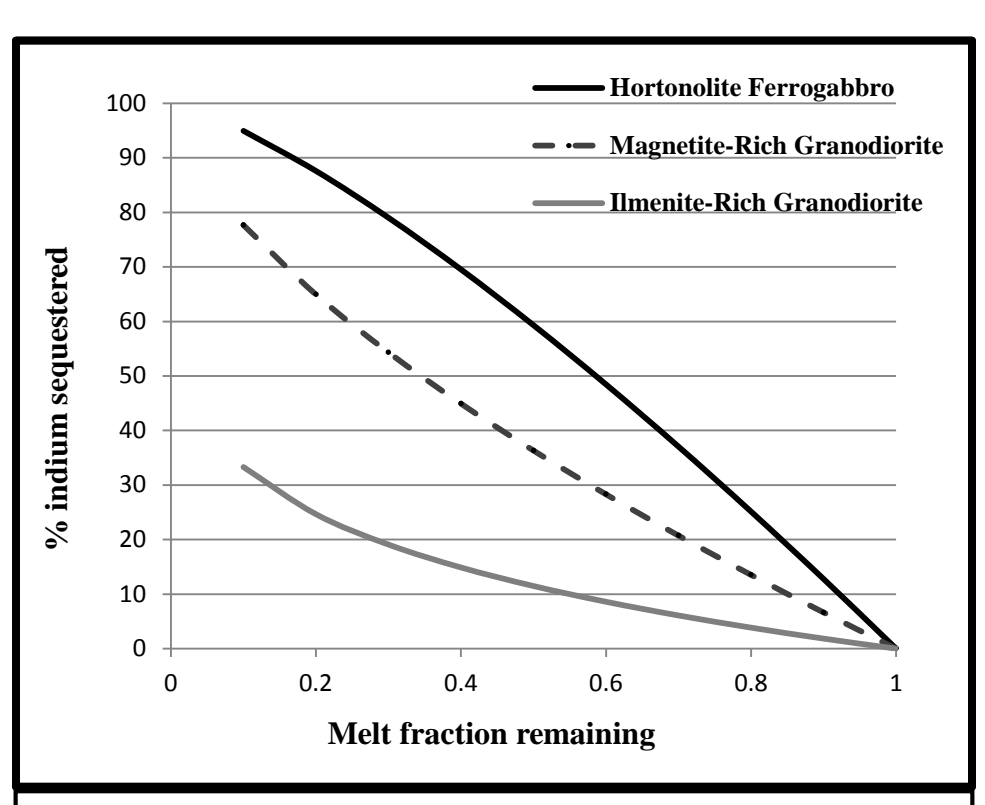


Figure 7. The fraction of indium in magma that is sequestered by varying modal abundance of crystalline phases.

sequestered by the crystalline phases. The percent indium sequestered by the crystalline phases as a function of melt fraction remaining is provided in Figure 7. The upper limit concentration of indium in the ore fluid at 83% crystallization is 4.2 ppm.

Minerals	Modal Abundance%	[In] (ppm)	Mass Fraction %	$D_{In}^{rac{mineral}{melt}}$	$D_{In}^{rac{mineral}{melt}} imes rac{Mass}{Fraction}$	\overline{D}
Plagioclase	45	0.0032	46	0.06	0.026	
Quartz	42	0.0032	41	0.06	0.023	
Alkali Feldspar	10	0.0032	10	0.06	0.006	0.18
Fe-Mg Silicates	2	0.23	2	4.1	0.094	0.10
Magnetite	0	0.16	0	2.9	0	
Ilmenite	0.3	0.29	1	5.2	0.03	
Chilled Marg	0.056					

Table 8. Modal abundance of minerals comprising an ilmenite-rich hornblende-biotite granodiorite. The chilled marginal gabbro is assumed to be the original melt composition. Concentrations and modal abundance data from Shimizu (1986).

As a magma undergoes fractionation, of phases such as magnetite, ilmentite, and ferromagnesian minerals, compositionally-evolved melts may ascend to higher levels of the crust while some proportion of solid phases remain at depth. Indium that is partitioned from the melt to these crystallizing phases may not be transported in the ascending melt phase. Therefore the amount indium available to form an ore deposit may be a primary function of the proportion of magnetite, ilmentite and ferromagnesian minerals that crystallize and remain in a magmatic-hydrothermal system. The model data presented above allows us to place calculated upper limits on the effect that crystallizing phases have on the indium budget of a magmatic system, and demonstrates that the effect of indium sequestration is greatest in the ferrogabbro than in the magnetite or ilmenite rich granodiorite. The concentration of indium in the ore fluid from a ferromagnesian rich system is on the order of 0.56 ppm. A melt that has a chemical composition that yields a magnetite rich granodiorite generates an ore fluid with an indium concentration of \approx 2.2 ppm. An ilmenite rich granodiorite yields an ore fluid that has an indium concentration of 4.2 ppm. As the modal abundances of ferromagnesian decrease the concentration of indium in the ore fluid increases.

Zhang et al., (2007), using an Inductively Coupled Plasma Mass Spectrometer measured the concentration of indium in fluid inclusions present in quartz from varying indium-rich and-poor ore deposits in China. The quartz crystallized at the main stage of mineralization of several In-rich and In-poor deposits and coexisted with sphalerite. The indium concentration in the fluid inclusions can be taken as the concentration of indium in the ore fluid. Zhang et al., 2007 cites the concentration of indium in the ore fluid for indium-rich ore deposits is 1.9 to 4.1 ppm. These concentrations coincide with model data presented above for the magnetite- and ilmenite- rich granodiorites. The hortonolite ferrogabbro does not fit into the cited literature for indium-rich ore fluid concentration which validates the idea that a ferromagnesian rich system will not be efficient in producing an ore deposit.

Conclusion

In conclusion this study demonstrates two important characteristics of indium in magmatic conditions. First, at 800°C and 100 MPa, the partition coefficient for indium between pyrrhotite and silicate melt is approximately 4. Second, in a pyrrhotite-saturated silicate melt pyrrhotite alone is not capable of sequestering indium. These two factors can be used as the base for future studies in better understanding the behavior of indium. Future experiments include considering the partition coefficient for indium between vapor and melt along with looking into the effects of magnetite alone on the sequestration of indium.

The model data presented in this study allow for an upper limit to be placed on the indium budget, and suggest strategies for the exploration for indium-bearing, magmatic-hydrothermal deposits. The average concentration of indium in an evolving ore fluid will increase progressing from ferromagnesian-rich basaltic systems to a magnetite-rich, and finally magnetite-absent, ilmentite-bearing felsic systems. Further, the efficiency with which indium is removed from the melt will increase as the water content of the melt increases, although the concentration of indium in the ore fluid will decrease.

References Cited

- Audetat, A. and Pettke, T. 2006, Evolution of a porphyry-Cu mineralized magma system at Santa Rita, New Mexico, USA: Journal of Petrology, v. 47, no. 10, p. 2021-2046.
- Burnham, C.W., 1979, Magmas and hydrothermal fluids, *in* Barnes, H.L., ed., Geochemistry of hydrothermal ore deposits: New York, Wiley, p. 71-136.
- Candela, P. A., 1986, The evolution of aqueous vapor from silicate melts: effect on oxygen fugacity: Geochimica et Cosmochimica Acta, v. 50, no. 6, p. 1205-1211.
- Candela, P. A. and Piccoli, P.M., 2005, Magmatic processes in the development of porphyrytype ore systems: Economic Geology, v. 100, p. 25-37.
- Candela, P. A., 1991, Physics of aqueous phase evolution in plutonic environments: American Mineralogist, v. 76, p. 1081-1091
- Englander, L., 2005, An experimental study of silver partitioning in sulfide-oxide-melt systems at 800 degrees C.: College Park, University of Maryland [Master's thesis], 144 p.
- Hedenquist, J.W. and Lowenstern, J.B., 1994, The role of magmas in the formation of hydrothermal ore deposits: Nature, v. 370, no. 6490, p. 519-527.
- Holland, H.D., 1972, Granites, solutions, and base metal deposits.: Economic Geology, v. 67, no. 3, p. 281-301.
- Ishihara, S., Hoshino, K., Murakami, H. and Endo, Y., 2006, Resource evaluation and some genetic aspects of indium in the Japanese ore deposits: Resource Geology v. 56, no. 3, p. 347-364.
- Ishihara, S. and Endo, Y., 2007, Indium and other trace elements in volcanogenic massive sulfide ores from the Kuroko, Besshi and other types in Japan: Bull. Geol. Surv. Japan ,v. 58, p. 7-22.
- Jorgenson, J. D. and George., M.W., 2005, Mineral Commodity Profile, Indium. US Geological Survey, 2005.
- Jugo, P.J., 1997, Experimental Study of the behavior of copper and gold in the system haplogranite—CuFeS₂-FeS-Au-H₂O-HCl-O₂-S₂ at 850 degrees C and 100 MPa: College Park, University of Maryland [Master's thesis], 93 p.
- Jugo, P. J., Candela, P.A., and Piccoli, P.M., 1999, Magmatic sulfides and Au: Cu ratios in porphyry deposits: an experimental study of copper and gold partitioning at 850 C, 100 MPa in a haplogranitic melt–pyrrhotite–intermediate solid solution–gold metal assemblage, at gas saturation: Lithos, v. 46, no. 3, p. 573-589.
- Keith, J.D., Dallmeyer, R.D., Kim, C., and Kowallis, B.J., 1991, The volcanic history and magmatic sulfide mineralogy of latites of the central East Tintic Mountains, Utah: Geology and Ore Deposits of the Great Basin: Geological Society of Nevada, Reno, NV, p. 461-483.
- Luhr, J. F., 1990, Experimental phase relations of water-and sulfur-saturated arc magmas and the 1982 eruptions of El Chichón volcano. Journal of Petrology, v. 31, no. 5, p. 1071-1114.
- McIntire, W. L., 1963, Trace element partition coefficients—a review of theory and applications to geology: Geochimica et Cosmochimica Acta, v. 27, no. 12, p. 1209-1264.
- Mengason, M. J., Piccoli, P. M., & Candela, P., 2010, An evaluation of the effect of copper on the estimation of sulfur fugacity (fS2) from pyrrhotite composition, Economic Geology, v. 105 n. 6, p. 1163-1169.
- Naney, M.T., 1983, Phase equilibria of rock-forming ferromagnesian silicates in granitic systems: American journal of science, v. 283, no. 10, p. 993-1033.

- Ohta, E., 1991, Polymetallic mineralization at the Toyoha mine, Hokkaido, Japan [PhD diss.]: Hoikkado, Hoikkado University, 138 p.
- Richards, J.P., McCulloch, M.T., Chappell, B.W., and Kerrich, R., 1991, Sources of metals in the Porgera gold deposit, Papua New Guinea: evidence from alteration, isotope, and noble metal geochemistry: Geochimica et Cosmochimica Acta, v. 55, no. 2, p. 565-580.
- Schwarz-Schampera, U., and Herzig, P.M., 2002, Indium: geology, mineralogy, and economics: Springer, 200 p.
- Seward, T. M., Henderson, C.M.B., and Charnock, J.M., 2000, Indium (III) chloride complexing and solvation in hydrothermal solutions to 350 C: an EXAFS study: Chemical Geology, v. 167, no. 1, p. 117-127.
- Shimizu, M., 1986, The Tokuwa batholith, Central Japan: An example of occurrence of ilmenite-series and magnetite-series granitoids in a batholith. University Museum, University of Tokyo.
- Simon, A. C., Pettke, T., Candela, P. A., Piccoli, P. M., & Heinrich, C. A., 2003, Experimental determination of Au solubility in rhyolite melt and magnetite: Constraints on magmatic Au budgets, American Mineralogist, v. 88, no. 11-12, p. 1644-1651.
- Simon, A.C., Pettke, T., Candela, P.C., Piccoli, P.M., and Heinrich, C.A., 2006, Copper partitioning in a melt–vapor–brine–magnetite–pyrrhotite assemblage, Geochimica et Cosmochimica Acta v.70, no. 22, p. 5583-5600.
- Sinclair, W. D., Kooiman, J.G.A., Martin, D.A., and Kjarsgaard, I.M., 2006, Geology, geochemistry and mineralogy of indium resources at Mount Pleasant, New Brunswick, Canada: Ore Geology Reviews, v. 28, no. 1, p. 123-145.
- Speer, A. J., 1987, Evolution of magmatic AFM mineral assemblages in granitoid rocks: the hornblende+ melt= biotite reaction in the Liberty Hill pluton, South Carolina: Am. Mineral (United States), v. 72, p. 863-878.
- Tattich, B.C., Candela, P.A., Piccoli, P.M., and Bodnar, R.J., 2009, Interpretation of H₂O/CO₂/NaCl phase equilibria in experiments at magmatic temperatures and pressures: Geological Society of America Abstracts with Programs, v. 41, no. 7, p. 332.
- Tattich, B.C., 2012, The Effect of CO₂ on copper partitioning in sulfur-free and sulfur-bearing felsic melt-vapor-brine assemblages: College Park, University of Maryland [PhD diss.], 207 p.
- Toulmin, P., and Barton, P.B., 1964, A thermodynamic study of pyrite and pyrrhotite: Geochimica et Cosmochimica Acta, v. 28, no. 5, p. 641-671.
- U.S. Geological Survey, 2005, Indium statistics, *in* Kelly, T.D., and Matos, G.R., comps., Historical statistics for mineral and material commodities in the United States: U.S. Geological Survey Data Series 140: http://pubs.usgs.gov/ds/2005/140/ (accessed April 2013).
- Wager, L. R., van Smit R, and Irving, H., 1958, Indium content of rocks and minerals from the Skaergaard intrusion, East Greenland: Geochimica et Cosmochimica Acta, v.13, no. 2, p. 81-86.
- Whitney, J. A., and Stormer, J.C., 1983, Igneous sulfides in the Fish Canyon Tuff and the role of sulfur in calc-alkaline magmas: Geology v. 11, no. 2, p.99-102.
- Yi, W., Halliday, A.N., Lee, D., and Christensen, J.N., 1995, Indium and tin in basalts, sulfides, and the mantle: Geochimica et Cosmochimica Acta, v. 59, no. 24, p. 5081-5090.
- Zellmer, G. F., & Annen, C., 2008, An introduction to magma dynamics, Geological Society, London, Special Publications, v. 304 n. 1, p. 1-13.

Zhang Qian, Zhu Xiaoqing, He Yuliang and Zhu Zhaohui., 2007, In, Sn, Pb and Zn Contents and Their Relationships in Ore-forming Fluids from Some In-rich and In-poor Deposits in China. Acta Geologica Sinica-English Edition, v. 81, no. 3, p. 450-462.

Appendix A. Detection limits for elements analyzed in glass and pyrrhotite.

Glass

Element	Detection limit (wt %)
Si	0.05
Al	0.04
Fe	0.07
Mn	0.08
Mg	0.06
Ca	0.02
Na	0.09
K	0.02
S	0.03
Cl	
In	0.0018

Pyrrhotite

Element	Detection limit (ppm)
Fe	100
S	20
In	30

Appendix B. EPMA analysis of starting pyrrhotite.

	S	Fe	Total
	40.55	59.14	99.68
	40.91	59.14	100.05
	40.75	58.78	99.53
	40.25	58.65	98.91
	40.87	58.99	99.86
AVG	40.67	58.94	99.61
STD	0.27	0.22	0.44

Appendix C. Composition of glass run products

104	SiO ₂	Al ₂ O ₃	Na₂O	K₂O	CaO	FeO	MnO	MgO	SO₃	Cl	In	Total	ASI
	77.12	10.57	4.52	3.90	bd	0.24	bd	0.06	bd	0.01	0.042	96.47	0.91
	76.89	10.32	3.37	3.95	bd	0.52	bd	bd	bd	0.01	0.046	95.11	1.05
	74.18	11.26	2.97	4.19	bd	0.87	bd	bd	bd	bd	0.046	93.62	1.20
	75.58	10.99	3.44	4.01	bd	bd	0.10	bd	bd	bd	0.043	94.17	1.10
AVG	75.94	10.79	3.58	4.01	bd	0.54	0.10	0.06	bd	0.01	0.044	94.84	1.06
STD	1.35	0.42	0.66	0.13	0.02	0.32	0.10	0.06	bd	0.001	0.0019	1.25	0.12

105	SiO₂	Al ₂ O₃	Na₂O	K₂O	CaO	FeO	MnO	MgO	SO₃	Cl	In	Total	ASI
	76.91	10.03	2.61	3.82	bd	0.10	0.02	bd	bd	0.03	0.0042	93.53	1.19
	73.73	12.10	2.88	4.56	bd	bd	bd	bd	0.01	0.03	0.0042	93.35	1.25
	73.77	12.02	2.98	4.42	bd	bd	0.03	bd	0.04	bd	0.0073	93.26	1.24
	73.66	11.75	3.83	4.55	bd	bd	0.06	0.08	0.03	0.03	0.0068	93.99	1.05
AVG	74.52	11.47	3.07	4.34	bd	0.10	0.04	0.08	0.03	0.03	0.0056	93.53	1.18
STD	1.59	0.98	0.52	0.35	bd	0.10	0.02	0.08	0.01	0.001	0.0016	0.32	0.09

122	SiO ₂	Al ₂ O ₃	Na₂O	K₂O	CaO	FeO	MnO	MgO	SO₃	CI	In	Total	ASI
	75.82	11.64	4.19	4.54	0.02	0.06	0.00	0.01	0.00	0.00	0.0185	96.32	0.98
	75.16	10.94	3.97	4.45	0.03	0.00	0.02	0.00	0.04	0.01	0.0139	94.62	0.96
	75.76	10.74	3.92	4.39	0.02	0.00	0.00	0.01	0.01	0.01	0.0119	94.88	0.95
	73.33	11.77	4.30	4.58	0.00	0.00	0.00	0.02	0.03	0.00	0.0108	94.04	0.98
	75.20	11.12	3.96	4.36	0.02	0.10	0.00	0.00	0.02	0.00	0.0146	94.80	0.99
	77.17	10.58	3.69	4.18	0.00	0.07	0.06	0.04	0.02	0.03	0.0112	95.85	1.00
	75.72	11.55	4.19	4.43	0.00	0.06	0.00	0.01	0.04	0.02	0.0098	96.03	0.99
	74.97	11.68	4.21	4.54	0.02	0.00	0.02	0.01	0.04	0.02	0.0167	95.53	0.98
	76.15	11.20	4.00	4.29	0.02	0.02	0.00	0.00	0.00	0.00	0.0244	95.70	1.00

AVG	75.48	11.25	4.05	4.42	0.01	0.03	0.01	0.01	0.02	0.01	0.015	95.31	0.98
STD	1.04	0.44	0.19	0.13	0.01	0.04	0.02	0.01	0.02	0.01	0.0046	0.76	0.01

120	SiO₂	Al ₂ O ₃	Na₂O	K₂O	CaO	FeO	MnO	MgO	SO₃	Cl	In	Total	ASI
	76.05	11.37	4.13	4.53	0.01	0.01	0.00	0.00	0.02	0.01	0.0469	96.17	0.97
	76.12	11.21	4.07	4.42	0.00	0.00	0.00	0.01	0.01	0.01	0.0483	95.90	0.98
	75.95	10.81	3.72	4.25	0.00	0.02	0.00	0.00	0.01	0.02	0.0469	94.83	1.01
	74.81	11.69	4.33	4.48	0.02	0.04	0.04	0.00	0.02	0.02	0.0337	95.46	0.97
	76.41	10.95	3.94	4.29	0.00	0.00	0.05	0.01	0.03	0.00	0.0256	95.71	0.98
	75.82	11.16	3.82	4.15	0.01	0.00	0.03	0.00	0.03	0.00	0.0157	95.04	1.03
	75.88	10.87	3.88	4.08	0.02	0.10	0.00	0.02	0.03	0.00	0.0171	94.91	1.00
	75.91	11.07	4.00	4.13	0.01	0.03	0.07	0.00	0.00	0.00	0.0217	95.23	1.00
	76.33	10.78	3.86	4.07	0.01	0.20	0.00	0.03	0.00	0.00	0.0257	95.32	1.00
	76.29	10.65	3.80	4.04	0.00	0.12	0.00	0.00	0.02	0.02	0.0337	94.97	1.00
AVG	75.96	11.06	3.95	4.24	0.01	0.05	0.02	0.01	0.02	0.01	0.032	95.36	1.00
STD	0.45	0.31	0.18	0.18	0.01	0.07	0.03	0.01	0.01	0.01	0.012	0.45	0.02

107	SiO ₂	Al ₂ O ₃	Na₂O	K₂O	CaO	FeO	MnO	MgO	SO₃	Cl	In	Total	ASI
	77.89	10.96	4.24	4.95	0.04	0.58	0.00	0.01	0.05	0.17	0.049	98.844	0.88
	73.27	10.23	4.21	5.02	0.00	0.52	0.00	0.00	0.05	0.54	0.049	94.278	0.83
AVG	75.58	10.60	4.22	4.99	0.02	0.55	0.00	0.01	0.05	0.36	0.049	96.56	0.86
STD	3.26	0.52	0.02	0.05	0.03	0.04	0.00	0.01	0.00	0.26	0.000	3.23	0.04

110	SiO₂	Al ₂ O ₃	Na₂O	K₂O	CaO	FeO	MnO	MgO	SO₃	Cl	In	Total	ASI
	72.70	11.40	4.69	5.07	bd	0.09	0.00	0.08	0.03	0.17	0.025	94.17	0.86
	75.98	10.04	3.94	4.92	0.02	0.25	0.16	0.08	0.01	0.13	0.028	95.50	0.85
	72.31	12.29	4.84	5.39	bd	0.58	0.06	0.00	0.06	0.20	0.046	95.69	0.89
	71.63	13.07	5.11	5.54	bd	0.64	0.00	0.00	0.00	0.17	0.037	96.12	0.91
	74.96	10.65	4.03	5.09	0.06	0.00	0.00	0.00	0.03	0.28	0.027	95.05	0.87
	75.81	10.51	3.92	5.20	bd	0.95	0.00	0.00	0.00	0.18	0.055	96.54	0.87
	75.32	10.46	4.40	5.09	0.02	0.69	0.10	0.02	0.05	0.17	0.114	96.28	0.82
	73.11	12.28	5.31	5.31	bd	0.13	0.16	0.00	0.02	0.18	0.048	96.46	0.85
Average	73.98	11.34	4.53	5.20	0.04	0.42	0.06	0.02	0.03	0.18	0.048	95.73	0.86
STD	1.72	1.10	0.54	0.20	0.02	0.34	0.07	0.04	0.02	0.04	0.029	0.81	0.03

109	SiO₂	Al₂O₃	Na₂O	K₂O	CaO	FeO	MnO	MgO	SO₃	Cl	In	Total	ASI
	74.44	10.20	3.18	4.88	bd	1.09	bd	bd	0.03	0.16	0.060	94.05	0.97
	73.67	9.65	4.11	4.47	bd	1.08	0.05	bd	0.02	0.12	0.054	93.22	0.83
	74.55	10.10	3.09	5.08	bd	1.10	bd	bd	0.05	0.22	0.058	94.26	0.96
	75.12	10.33	4.28	4.76	bd	1.22	bd	bd	bd	0.19	0.060	95.97	0.85
	74.98	10.74	3.60	4.74	bd	1.29	bd	0.02	0.01	0.22	0.072	95.69	0.97
AVG	74.55	10.20	3.65	4.79	bd	1.16	0.05	0.02	0.03	0.18	0.076	94.64	0.92
STD	0.57	0.39	0.53	0.22	bd	0.10	0.05	0.02	0.02	0.04	0.014	1.16	0.07

113	SiO ₂	Al ₂ O ₃	Na₂O	K₂O	CaO	FeO	MnO	MgO	SO₃	Cl	In	Total	ASI
	74.00	11.01	4.31	5.17	0.01	0.91	0.05	0.00	0.05	0.21	0.050	95.67	0.87
	73.65	10.71	4.21	4.92	0.04	0.88	0.00	0.04	0.00	0.17	0.051	94.58	0.87
	75.78	10.04	4.05	4.70	bd	0.82	0.03	0.00	0.00	0.16	0.065	95.54	0.86
	74.86	10.44	4.36	4.90	bd	0.60	0.00	0.01	0.00	0.18	0.061	95.30	0.84
	74.60	9.99	3.97	4.87	0.02	0.60	0.02	0.02	0.00	0.20	0.061	94.24	0.84
	75.50	10.95	4.57	5.14	0.03	0.50	0.00	0.10	0.00	0.13	0.056	96.89	0.83

	75.16	10.91	4.66	5.04	0.01	0.96	0.00	0.01	0.00	0.21	0.046	96.91	0.83
	75.06	10.95	4.30	4.91	bd	0.47	0.04	0.00	0.01	0.18	0.061	95.89	0.88
	74.71	11.32	4.46	5.09	bd	0.85	0.02	0.05	0.05	0.20	0.051	96.69	0.88
	73.57	10.84	4.70	4.90	0.06	1.02	0.00	0.00	0.04	0.23	0.048	95.32	0.82
	74.61	10.98	4.36	5.01	0.01	0.88	0.00	0.00	0.00	0.20	0.062	95.99	0.87
	72.15	11.99	5.02	5.68	0.03	1.23	0.00	0.00	0.05	0.23	0.054	96.32	0.83
	75.68	10.83	4.46	4.97	0.02	0.81	0.00	0.04	0.03	0.18	0.066	96.97	0.85
	73.72	11.09	4.79	5.18	0.03	0.86	0.00	0.02	0.00	0.20	0.064	95.84	0.82
	75.47	10.61	4.29	5.05	bd	0.85	0.00	0.04	0.04	0.20	0.062	96.51	0.85
	74.12	11.50	4.68	5.35	0.03	0.85	0.05	0.07	0.02	0.19	0.047	96.82	0.85
	74.11	10.86	4.70	5.00	bd	1.08	0.00	0.00	0.00	0.19	0.051	95.90	0.83
	73.86	10.94	4.37	5.09	0.03	0.71	0.02	0.06	0.04	0.18	0.056	95.26	0.86
Average	74.48	10.89	4.46	5.05	0.03	0.83	0.01	0.03	0.02	0.19	0.056	95.92	0.85
STD	0.93	0.46	0.27	0.21	0.01	0.20	0.02	0.03	0.02	0.02	0.0066	0.80	0.02

115	SiO₂	Al ₂ O ₃	Na₂O	K₂O	CaO	FeO	MnO	MgO	SO₃	CI	In	Total	ASI
	74.55	10.98	3.72	5.00	0.02	0.83	0.00	0.00	0.05	0.16	0.070	95.38	0.95
	74.37	10.78	3.59	4.91	0.00	0.79	0.02	0.00	0.00	0.16	0.071	94.69	0.96
	74.62	11.06	3.92	5.05	0.00	0.76	0.00	0.00	0.04	0.16	0.079	95.68	0.93
	74.28	10.73	3.83	5.09	0.03	0.82	0.00	0.00	0.05	0.16	0.072	95.07	0.91
	74.26	10.52	3.31	4.79	0.01	0.82	0.00	0.00	0.05	0.14	0.062	93.95	0.99
	73.43	11.91	4.09	5.19	0.00	0.68	0.01	0.00	0.07	0.19	0.068	95.64	0.96
	73.88	11.49	3.90	5.22	0.03	0.72	0.00	0.00	0.04	0.16	0.055	95.50	0.95
Average	74.20	11.06	3.77	5.04	0.01	0.77	0.00	0.00	0.04	0.16	0.068	95.13	0.95
STD	0.41	0.48	0.26	0.15	0.01	0.06	0.01	0.00	0.02	0.01	0.008	0.63	0.03

MnO

MgO

SO₃

Total

ASI

Al₂O₃

SiO₂

116

Na₂O

K₂O

CaO

FeO

	74.68	10.04	3.84	4.98	0.01	1.68	0.00	0.01	0.00	0.30	0.073	95.61	0.86
	73.08	10.41	3.99	5.06	0.03	1.56	0.06	0.00	0.04	0.32	0.076	94.62	0.86
Average	73.88	10.23	3.91	5.02	0.02	1.62	0.03	0.00	0.02	0.31	0.074	95.12	0.86
STD	1.13	0.26	0.11	0.05	0.02	0.08	0.04	0.01	0.03	0.01	0.0017	0.70	0.00
117	SiO₂	Al ₂ O ₃	Na₂O	K₂O	CaO	FeO	MnO	MgO	SO₃	Cl	In	Total	ASI
	74.57	10.24	3.46	4.79	0.03	0.62	0.05	0.00	0.02	0.02	0.052	93.85	0.94
	74.31	10.94	3.61	4.89	0.01	0.52	0.03	0.00	0.04	0.04	0.044	94.44	0.97
	75.88	10.28	3.29	4.55	0.02	0.67	0.00	0.01	0.00	0.00	0.040	94.72	0.99
	74.62	10.27	3.43	4.79	0.00	0.67	0.00	0.00	0.02	0.02	0.052	93.87	0.95
Average	74.84	10.43	3.45	4.76	0.01	0.62	0.02	0.00	0.02	0.02	0.047	94.22	0.96
STD	0.70	0.34	0.13	0.15	0.01	0.07	0.02	0.00	0.02	0.02	0.0059	0.43	0.02
											1		
118	SiO₂	Al ₂ O ₃	Na₂O	K₂O	CaO	FeO	MnO	MgO	SO₃	Cl	In	Total	ASI
	73.91	10.29	3.91	4.74	0.02	0.74	0.06	0.00	0.00	0.27	0.038	93.98	0.89
	73.92	11.08	4.17	5.12	0.00	0.73	0.04	0.00	0.02	0.26	0.041	95.37	0.89
Average	73.91	10.69	4.04	4.93	0.01	0.74	0.05	0.00	0.01	0.27	0.039	94.67	0.89
STD	0.003	0.56	0.18	0.27	0.01	0.01	0.02	0.00	0.01	0.01	0.0023	0.98	0.002
119	SiO₂	Al ₂ O ₃	Na₂O	K₂O	CaO	FeO	MnO	MgO	SO₃	Cl	In	Total	ASI
119	SIU ₂	Al ₂ U ₃	Na ₂ U	N ₂ U	CaU	reu	IVIIIU	IVIBO	3∪3	CI	ın	Total	ASI

119	SiO ₂	Al ₂ O ₃	Na₂O	K₂O	CaO	FeO	MnO	MgO	SO₃	Cl	In	Total	ASI
	75.84	10.94	3.77	4.99	0.000	0.37	0.00	0.00	0.00	0.19	0.020	96.12	0.94
	75.69	10.82	3.69	4.89	0.021	0.38	0.07	0.02	0.03	0.18	0.018	95.80	0.95
	76.57	10.55	3.79	4.85	0.004	0.49	0.05	0.03	0.01	0.20	0.019	96.55	0.92
	73.76	11.69	4.18	5.22	0.008	0.60	0.05	0.01	0.00	0.23	0.017	95.76	0.93

	73.94	11.15	3.84	5.06	0.011	0.61	0.05	0.00	0.01	0.22	0.018	94.91	0.94
	73.91	11.15	4.07	5.17	0.043	1.50	0.07	0.01	0.00	0.17	0.018	96.13	0.90
	72.92	10.47	3.89	4.97	0.024	1.54	0.06	0.00	0.01	0.17	0.023	94.07	0.89
	73.96	10.92	3.96	5.13	0.033	1.41	0.02	0.01	0.01	0.17	0.021	95.66	0.90
	73.77	10.77	4.04	5.10	0.018	1.46	0.01	0.00	0.01	0.18	0.021	95.37	0.88
Average	74.49	10.94	3.91	5.04	0.02	0.93	0.04	0.01	0.01	0.19	0.020	95.59	0.92
STD	1.23	0.37	0.16	0.13	0.01	0.53	0.02	0.01	0.01	0.02	0.0019	0.74	0.03

121	SiO₂	Al ₂ O₃	Na₂O	K₂O	CaO	FeO	MnO	MgO	SO₃	Cl	In	Total	ASI
	76.47	10.66	3.52	4.76	0.00	0.30	0.00	0.00	0.05	0.14	0.035	95.94	0.97
	76.01	10.71	3.48	4.77	0.00	0.39	0.00	0.00	0.04	0.14	0.037	95.58	0.98
	75.57	11.04	3.61	4.91	0.01	0.35	0.03	0.00	0.04	0.13	0.040	95.72	0.98
	75.34	11.53	3.75	4.99	0.00	0.26	0.06	0.00	0.06	0.13	0.041	96.16	1.00
	76.14	11.19	3.62	4.94	0.01	0.19	0.00	0.00	0.03	0.13	0.039	96.30	0.99
	75.48	11.29	3.67	4.99	0.02	0.22	0.02	0.02	0.10	0.13	0.041	95.99	0.98
Average	75.84	11.07	3.61	4.89	0.01	0.28	0.02	0.00	0.05	0.13	0.039	95.95	0.98
STD	0.44	0.34	0.10	0.11	0.01	0.07	0.02	0.01	0.02	0.01	0.0021	0.27	0.01

Appendix D. Composition of pyrrhotite run products

104	S	Fe	In	Total	Moles S	Moles Fe	Moles In	N
	39.13	59.97	0.30	99.40	1.22	1.07	0.0027	0.94
	41.30	58.69	0.34	100.33	1.29	1.05	0.0029	0.90
	39.42	61.03	0.21	100.67	1.23	1.09	0.0019	0.94
AVG	39.95	59.90	0.29	100.13	1.25	1.07	0.0025	0.93
STD	1.18	1.17	0.063	0.65	0.04	0.02	0.0006	0.02

105	S	Fe	In	Total	Moles S	Moles Fe	Moles In	N
	41.16	58.86	0.11	100.12	1.28	1.05	0.0009	0.90
	40.84	59.50	0.21	100.55	1.27	1.07	0.0018	0.91
	41.10	59.38	0.17	100.64	1.28	1.06	0.0015	0.91
	37.82	60.58	0.16	98.56	1.18	1.08	0.0014	0.96
	40.66	59.06	0.16	99.88	1.27	1.06	0.0014	0.91
	37.82	61.35	0.15	99.32	1.18	1.10	0.0013	0.96
AVG	39.90	59.79	0.16	99.85	1.24	1.07	0.00	0.93
STD	1.62	0.97	0.033	0.79	0.05	0.02	0.00029	0.03

122	S	Fe	In	Total	Moles S	Moles Fe	Moles In	N
	40.91	60.08	0.15	101.14	1.28	1.08	0.0013	0.91
	41.36	60.24	0.15	101.76	1.29	1.08	0.0013	0.91
	40.20	59.84	0.16	100.20	1.25	1.07	0.0014	0.92
	41.54	60.04	0.18	101.76	1.30	1.08	0.0015	0.91
	40.75	59.97	0.20	100.92	1.27	1.07	0.0018	0.92
	41.11	60.11	0.19	101.41	1.28	1.08	0.0016	0.91
	40.67	59.98	0.19	100.84	1.268665	1.074171	0.001634	0.92
	41.32	60.18	0.20	101.70	1.28893	1.077745	0.001746	0.91

AVG	40.98	60.06	0.18	101.22	1.28	1.08	0.0015	0.91
STD	0.44	0.13	0.022	0.55	0.01	0.00	0.00019	0.00

120	S	Fe	In	Total	Moles S	Moles Fe	Moles In	N
	39.14	60.51	0.20	99.86	1.22	1.08	0.0017	0.94
	38.96	60.32	0.26	99.57	1.22	1.08	0.0022	0.94
	38.12	59.65	0.30	98.10	1.19	1.07	0.0026	0.95
	39.20	60.21	0.34	99.77	1.22	1.08	0.0029	0.94
	38.08	59.86	0.32	98.27	1.19	1.07	0.0028	0.95
	38.53	60.04	0.33	98.92	1.20	1.08	0.0029	0.94
	38.25	59.96	0.31	98.53	1.19	1.07	0.0027	0.95
	38.61	60.08	0.29	99.00	1.20	1.08	0.0026	0.94
AVG	38.61	60.08	0.29	99.00	1.20	1.08	0.0026	0.94
STD	0.45	0.27	0.045	0.68	0.01	0.00	0.00040	0.00

107	S	Fe	In	Total	moles S	Moles Fe	Moles In	N
	42.32	58.01	0.14	100.47	1.32	1.04	0.0012	0.88
	41.14	59.01	0.18	100.33	1.28	1.06	0.0016	0.90
	41.56	58.92	0.41	100.89	1.30	1.06	0.0036	0.90
	39.56	57.40	0.12	97.08	1.23	1.03	0.0010	0.91
	39.23	59.04	0.23	98.50	1.22	1.06	0.0020	0.93
AVG	40.76	58.48	0.22	99.45	1.27	1.05	0.0019	0.90
STD	1.32	0.74	0.12	1.61	0.04	0.01	0.0010	0.02

110	S	Fe	ln	Total	Moles S	Moles Fe	Moles In	N
	39.50	57.87	0.12	97.49	1.23	1.04	0.0011	0.91
	40.62	58.47	0.18	99.28	1.27	1.05	0.0016	0.90
	40.90	58.68	0.07	99.65	1.28	1.05	0.0006	0.90
	39.87	58.54	0.31	98.72	1.24	1.05	0.0027	0.91
	39.87	58.76	0.09	98.71	1.24	1.05	0.0008	0.92
	39.75	58.56	0.09	98.40	1.24	1.05	0.0008	0.92
	39.13	59.08	0.17	98.38	1.22	1.06	0.0014	0.93
	38.73	59.30	0.12	98.15	1.21	1.06	0.0010	0.94
	38.74	58.72	0.13	97.59	1.21	1.05	0.0011	0.93
	39.51	57.32	0.13	96.97	1.23	1.03	0.0011	0.91
Average	39.66	58.53	0.14	98.33	1.24	1.05	0.0012	0.92
STD	0.68	0.54	0.065	0.78	0.02	0.01	0.0006	0.01

109	S	Fe	In	Total	Moles S	Moles Fe	Moles In	N
	41.36	59.34	0.10	100.80	1.29	1.06	0.00	0.90
	39.04	59.90	0.20	99.14	1.22	1.07	0.00	0.94
	41.78	58.45	0.20	100.43	1.30	1.05	0.00	0.89
	42.24	58.15	0.21	100.60	1.32	1.04	0.00	0.88
	40.20	58.89	0.11	99.20	1.25	1.05	0.00	0.91
AVG	40.92	58.95	0.16	100.03	1.28	1.06	0.0014	0.91
STD	1.30	0.70	0.055	0.80	0.04	0.01	0.00048	0.02

113	S	Fe	In	Total	Moles S	Moles Fe	Moles In	N
	39.60	58.57	0.06	98.23	1.24	1.05	0.0005	0.92
	39.17	58.01	0.06	97.24	1.22	1.04	0.0005	0.92
	39.04	58.18	0.04	97.27	1.22	1.04	0.0004	0.92
	39.65	57.42	0.05	97.11	1.24	1.03	0.0004	0.91
	38.97	58.50	0.05	97.53	1.22	1.05	0.0004	0.93
	39.14	58.27	0.06	97.47	1.22	1.04	0.0005	0.92
	39.05	58.14	0.04	97.24	1.22	1.04	0.0003	0.92
Average	39.23	58.16	0.05	97.44	1.22	1.04	0.0004	0.92
STD	0.28	0.38	0.008	0.38	0.01	0.01	0.0001	0.01

115	S	Fe	In	Cu	Total	Moles S	Moles Fe	Moles In	Moles Cu
	39.81	57.74	0.16	0.03	97.71	1.24	1.03	0.0014	0.00041
	39.39	57.96	0.11	0.00	97.46	1.23	1.04	0.0010	0.00
	39.02	58.88	0.16	0.02	98.06	1.22	1.05	0.0014	0.00036
	39.54	58.22	0.11	0.03	97.87	1.23	1.04	0.0010	0.00039
	38.87	58.78	0.17	0.02	97.82	1.21	1.05	0.0015	0.00035
	38.54	58.71	0.17	0.02	97.42	1.20	1.05	0.0015	0.00037
	38.94	58.22	0.08	0.02	97.24	1.21	1.04	0.0007	0.00026
Average	39.16	58.36	0.14	0.02	97.65	1.22	1.05	0.0012	0.00031
STD	0.44	0.44	0.035	0.01	0.29	0.01	0.01	0.00031	0.00014

116	S	Fe	In	Cu	Total	Moles S	Moles Fe	Moles In	Moles Cu
	38.88	60.35	0.24	0.03	99.5	1.21	1.08	0.0021	0.00052
	38.94	60.43	0.19	0.02	99.6	1.21	1.08	0.0017	0.00
	38.46	60.18	0.15	0.02	98.8	1.20	1.08	0.0013	0.00033
	38.35	60.31	0.19	0.02	98.8	1.20	1.08	0.0017	0.00031
	38.58	60.24	0.21	0.03	99.0	1.20	1.08	0.0018	0.00046
	39.20	60.12	0.20	0.02	99.5	1.22	1.08	0.0018	0.00034
	38.62	60.21	0.36	0.02	99.2	1.20	1.08	0.0032	0.00038
	38.78	60.35	0.37	0.03	99.49	1.21	1.08	0.0032	0.00048
	38.82	60.35	0.23	0.01	99.40	1.21	1.08	0.0020	0.00022
	38.46	59.99	0.17	0.02	98.63	1.20	1.07	0.0015	0.00039
Average	38.71	60.25	0.23	0.02	99.19	1.21	1.08	0.00202	0.00038
STD	0.26	0.13	0.08	0.01	0.35	0.01	0.0023	0.00066	0.00009

117	S	Fe	In	Cu	Total	Moles S	Moles Fe	Moles In	Moles Cu
	40.13	58.86	0.18	0.02	99.17	1.25	1.05	0.0015	0.00026
	39.89	57.29	0.18	0.02	97.36	1.24	1.03	0.0016	0.00
	40.22	58.39	0.25	0.03	98.85	1.25	1.05	0.0022	0.00041
Average	40.08	58.18	0.20	0.02	98.46	1.25	1.04	0.0018	0.00035
STD	0.17	0.81	0.04	0.005	0.97	0.01	0.01	0.00037	0.00008

118	S	Fe	In	Cu	Total	Moles S	Moles Fe	Moles In	Moles Cu
	39.25	59.89	0.32	0.02	99.5	1.22	1.07	0.0028	0.00024
	39.27	59.96	0.24	0.01	99.5	1.22	1.07	0.0021	0.00
	39.29	59.86	0.47	0.01	99.6	1.23	1.07	0.0041	0.00020
	39.06	59.65	0.22	0.02	98.9	1.22	1.07	0.0019	0.00029
	39.23	59.73	0.29	0.02	99.2	1.22	1.07	0.0025	0.00037

	39.51	60.12	0.14	0.03	99.8	1.23	1.08	0.0012	0.00049
	39.24	60.22	0.40	0.02	99.9	1.22	1.08	0.0035	0.00034
	39.14	60.04	0.33	0.01	99.5	1.22	1.08	0.0029	0.00019
	39.25	59.67	0.39	0.02	99.3	1.22	1.07	0.0034	0.00031
	39.33	60.08	0.31	0.02	99.7	1.23	1.08	0.0027	0.00026
Average	39.22	59.82	0.31	0.02	99.3	1.22	1.07	0.0027	0.00025
STD	0.09	0.12	0.10	0.005	0.27	0.00	0.00	0.00086	0.00008

119	S	Fe	In	Cu	Total	Moles S	Moles Fe	Moles In	Moles Cu
	38.14	61.46	0.017	0.03	99.65	1.19	1.10	0.0002	0.00043
	38.82	61.23	0.023	0.01	100.09	1.21	1.10	0.0002	0.00
	36.05	60.04	0.022	0.00	96.11	1.12	1.08	0.0002	0.00000
	37.54	60.37	0.022	0.01	97.94	1.17	1.08	0.0002	0.00022
	37.41	59.77	0.022	0.00	97.20	1.17	1.07	0.0002	0.00006
	38.80	61.70	0.023	0.00	100.54	1.21	1.11	0.0002	0.00007
	39.02	61.70	0.018	0.01	100.75	1.22	1.10	0.0002	0.00017
	38.43	60.24	0.024	0.03	98.72	1.20	1.08	0.0002	0.00046
Average	38.03	60.82	0.021	0.01	98.87	1.19	1.09	0.00018	0.00020
STD	1.00	0.79	0.0025	0.01	1.68	0.03	0.01	0.000021	0.00017

121	S	Fe	In	Cu	Total	Moles S	Moles Fe	Moles In	Moles Cu
1	38.64	58.85	0.15	0.02	97.65	1.21	1.05	0.0013	0.00027
3	41.09	59.59	0.21	0.05	100.95	1.28	1.07	0.0019	0.00085
4	41.01	59.79	0.15	0.04	100.99	1.28	1.07	0.0013	0.00058
5	40.72	59.50	0.19	0.04	100.45	1.27	1.07	0.0017	0.00056

Average	40.37	59.43	0.18	0.04	100.01	1.26	1.06	0.0015	0.00057
STD	1.16	0.41	0.032	0.02	1.59	0.04	0.01	0.00028	0.00024

Appendix E

"I pledge on my honor that I have not given or received any unauthorized assistance on this assignment/exam"

Sean M Kayser